



Available online at www.sciencedirect.com

ScienceDirect

Comput. Methods Appl. Mech. Engrg. 415 (2023) 116290

**Computer methods
in applied
mechanics and
engineering**

www.elsevier.com/locate/cma

Physics-informed radial basis network (PIRBN): A local approximating neural network for solving nonlinear partial differential equations

Jinshuai Bai^{a,b,f}, Gui-Rong Liu^{c,*}, Ashish Gupta^{b,d,e}, Laith Alzubaidi^{a,b}, Xi-Qiao Feng^f, YuanTong Gu^{a,b,**}

^a School of Mechanical, Medical and Process Engineering, Queensland University of Technology, Brisbane, QLD 4000, Australia

^b ARC Industrial Transformation Training Centre—Joint Biomechanics, Queensland University of Technology, Brisbane, QLD 4000, Australia

^c Department of Aerospace Engineering and Engineering Mechanics, University of Cincinnati, OH 45221, USA

^d Queensland Unit for Advanced Shoulder Research, Brisbane, QLD, 4000, Australia

^e Greenslopes Private Hospital, Brisbane, QLD, 4120, Australia

^f Institute of Biomechanics and Medical Engineering, AML, Department of Engineering Mechanics, Tsinghua University, Beijing 100084, China

Received 23 April 2023; received in revised form 8 July 2023; accepted 17 July 2023

Available online 3 August 2023

Abstract

Our recent study has found that physics-informed neural networks (PINN) tend to be local approximators after training. This observation led to the development of a novel physics-informed radial basis network (PIRBN), which is capable of maintaining the local approximating property throughout the entire training process. Unlike deep neural networks, a PIRBN comprises only one hidden layer and a radial basis “activation” function. Under appropriate conditions, we demonstrated that the training of PIRBNs using gradient descendent methods can converge to Gaussian processes. Besides, we studied the training dynamics of PIRBN via the neural tangent kernel (NTK) theory. In addition, comprehensive investigations regarding the initialisation strategies of PIRBN were conducted. Numerical examples demonstrated that PIRBN is more effective than PINN in solving nonlinear partial differential equations with high-frequency features and ill-posed computational domains. Moreover, the existing PINN numerical techniques, such as adaptive learning, decomposition and different types of loss functions, are applicable to PIRBN. The programs that can regenerate all numerical results are available at <https://github.com/JinshuaiBai/PIRBN>.

© 2023 The Author(s). Published by Elsevier B.V. This is an open access article under the CC BY-NC-ND license (<http://creativecommons.org/licenses/by-nc-nd/4.0/>).

Keywords: Physics-informed neural network; Physics-informed radial basis network; Partial differential equations; Neural tangent kernel

1. Introduction

Deep learning (DL) techniques have been extensively used to solve partial differential equations (PDEs) over the past decade [1]. Among these, the physics-informed neural network (PINN) has earned increasing interest because it can be trained using both observation data (i.e. boundary conditions) and PDEs themselves [2]. By training neural

* Corresponding author.

** Corresponding author at: School of Mechanical, Medical and Process Engineering, Queensland University of Technology, Brisbane, QLD 4000, Australia.

E-mail addresses: liugr@ucmail.uc.edu (G.-R. Liu), yuantong.gu@qut.edu.au (Y. Gu).

networks with PDEs, PINN predictions show remarkable accuracy and excellent generalisation property [3]. Now, PINN has been widely applied to various systems that are governed by PDEs, including mechanics modelling [4–15], material exploration [16–23], and medical studies [24–34], to name but a few.

Despite its empirical success, PINN suffers from difficulties in solving PDEs with high-frequency features or have ill-posed computational domains [2,35], and thus great efforts have been witnessed in improving PINN. Choosing the appropriate physics laws to design effective physics-informed loss functions is one way to deal with the challenges [36]. Samaniego et al. [4] and Kharazmi et al. [37] formulated physics-informed loss functions for PINN training using the variational method. Haghigat et al. [38] and Yu et al. [39] embed not only PDEs but also gradient information obtained from sample points in the physics-informed loss function, rendering a significant enhancement in the performance of PINN for predicting gradient fields. Fuhg et al. [40] composed a mixed-form physics-informed loss function by integrating the variational formulation and PDEs. Bai et al. [41] integrated the weighted residual method to weaken the constraints from PDEs. Apart from the above, decomposition and transformation with regard to the computational domain is another way to address the challenges. Jagtap et al. [42] and Kharazmi et al. [37] divided computational domains into pieces. In their work, the solution of PDEs in each subdomain was predicted by a corresponding PINN. Dong and Li [43] proposed the local extreme learning framework that can ensure the continuity conditions among the decomposed domains. Based on the decomposition techniques, Shukla et al. [44] proposed a parallel computing technique to improve the training efficiency of PINNs. Nguyen-Thanh et al. [45] applied the isoparametric technique to pre-normalise complex computational domains into simple geometries. By using a distance-based encoding layer, Ramabathiran and Ramachandran [46] proposed sparse, physics-based, and partially interpretable neural networks (SPINN) that strengthen the interpretability of neural network for solving PDEs. The SPINN can be regarded as a generalised the meshless numerical method, while maintaining the powerful structure of DL models.

Recent advances in terms of the theoretical study of DL, the so-called neural tangent kernel (NTK) theory, have also shed light to PINN. The original NTK theory was proposed by Jacot et al. [47] and proved that training of infinite width neural networks with enough small learning rate can converge to Gaussian processes [48,49], which provided insights into DL training dynamics from the theoretical regard [50]. The NTK theory was then introduced to PINN by Wang et al. [51]. In their work, the training of PINN was analysed via the lens of NTK theory. More importantly, an NTK-based adaptive learning scheme was proposed to balance the loss terms automatically. With the help of the NTK-based adaptive learning scheme, different physics in PINNs can be equally trained and the PINNs can more effectively deal with problems that exhibit high-frequency features. Later, Wang et al. [52,53] reported the connection between the NTK and the spectral bias in PINN, and tuned neural network structures to address multi-scale problems and long-term evolution problems. Li et al. [54] analysed the error estimation of PINNs through the NTK theory. Xu et al. [55] studied the training dynamics of PINNs for inverse problems via the NTK theory and proposed a novel gradient descendent algorithm.

Inspired by the aforementioned studies, this work starts by studying the training dynamics of PINN via the NTK theory. By visualising the evolution of a PINN's NTK throughout training, we found that a PINN tends to be a local approximator after training. Besides, when coping with PDEs that exhibit high-frequency features or have ill-posed computational domains, PINN fails for predictions due to the difficulties of training PINN into a local approximator. Thus, based on this finding, we tailored a neural network structure, namely the physics-informed radial basis network (PIRBN), that naturally possesses the local approximation property. The main contributions of this work are summarised as follows:

- (i) From numerical experiments and the NTK theory, we found that PINNs tend to become local approximators during training via gradient descendent algorithms.
- (ii) Based on the above finding, we proposed the PIRBN, which has the local approximation property throughout the training.
- (iii) We prove that training the proposed PIRBN via gradient descendent algorithms also converges to Gaussian Processes when the width of the PIRBN tends to be infinite with an infinitesimal small learning rate.
- (iv) Comprehensive studies of the proposed PIRBN regarding parameter initialisation strategies, sizes of sample points and selections of radial basis activation functions are provided.
- (v) Challenging PDEs examples, which possess high-frequency features and ill-posed computational domains, are presented to show the performance of PIRBN with respect to PINN. Those problems that require domain decomposition techniques and multiple-layer PINNs can be now effectively solved by using single-layer PIRBNs.

The paper is organised as follows: In Section 2, the basic conceptions of PINN and the NTK theory for PINN are briefly recalled. Meanwhile, by visualising the NTK of PINN through training processes, the local approximation property of PINN is observed. In Section 3, based on the finding, the PIRBN is proposed and formulated. Besides, the training dynamics of PIRBN are analysed by the NTK theory and the initialisation strategies of PIRBN are discussed in detail. In Section 4, several numerical examples, which are challenging for PINN, are conducted to show the better performance of PIRBN. In Section 5, the main conclusions of this work are summarised, and future perspectives are provided.

2. A recap of PINN and NTK theory for PINN

2.1. Physics-informed neural network

We first recap the basic conceptions of the initial PINN [56]. Consider a set of PDEs with the boundary condition as

$$\begin{aligned} G[u] - g(\mathbf{x}^g) &= 0, \quad \text{for } \mathbf{x}^g \in \Omega, \\ B[u] - b(\mathbf{x}^b) &= 0, \quad \text{for } \mathbf{x}^b \in \partial\Omega, \end{aligned} \quad (1)$$

where $G[\cdot]$ is prescribed partial differential operators and $B[\cdot]$ is the boundary condition operator, $g(\mathbf{x})$ and $b(\mathbf{x})$ are given functions, Ω denotes the computational domain in \mathbb{R}^n , and $u(x): \mathbb{R}^n \rightarrow \mathbb{R}$ is the solution function governed by the PDE. To solve the PDE problem, a feedforward neural network (FNN) [11] is used to approximate the solution function as

$$u(\mathbf{x}) = F(\mathbf{x}, \boldsymbol{\theta}), \quad (2)$$

where $\boldsymbol{\theta}$ represents all the trainable parameters of the FNN. To train the FNN with physics, the physics-informed loss function is formulated as

$$\mathcal{L}(\boldsymbol{\theta}) = \mathcal{L}_g(\boldsymbol{\theta}) + \mathcal{L}_b(\boldsymbol{\theta}), \quad (3)$$

where \mathcal{L}_g and \mathcal{L}_b are the loss terms from the PDE and the boundary condition, respectively. They can be calculated by

$$\begin{aligned} \mathcal{L}_g(\boldsymbol{\theta}) &= \frac{1}{2} \sum_i^{n_g} |G[u(\mathbf{x}_i^g)] - g(\mathbf{x}_i^g)|^2, \\ \mathcal{L}_b(\boldsymbol{\theta}) &= \frac{1}{2} \sum_i^{n_b} |B[u(\mathbf{x}_i^b)] - b(\mathbf{x}_i^b)|^2, \end{aligned} \quad (4)$$

where n_g and n_b are the numbers of in-domain sample points and boundary sample points, respectively. More details regarding PINN can be found in [56].

2.2. Neural tangent kernel theory for physics-informed neural network

The neural tangent kernel (NTK) theory for PINN also is briefly recalled. Consider an infinite width PINN for solving a PDE shown as Eq. (1). A gradient descendent algorithm is selected as the training approach and all parameters in the network are initialised via the LeCun initialisation scheme [57]. In this manner, according to Wang et al. [51], the training process for such PINN can converge to independent and identically distributed (i.i.d.) centred Gaussian processes (\mathcal{GP})

$$\begin{aligned} \lim_{d \rightarrow \infty} G[u(\mathbf{x}; \boldsymbol{\theta}(t))] &\rightarrow \mathcal{GP}(0, \Sigma_g(\mathbf{x}, \mathbf{x}')), \\ \lim_{d \rightarrow \infty} B[u(\mathbf{x}; \boldsymbol{\theta}(t))] &\rightarrow \mathcal{GP}(0, \Sigma_b(\mathbf{x}, \mathbf{x}')), \end{aligned} \quad (5)$$

where d denotes the width (number of neurons in each hidden layer) of PINN, t denotes the training time [51], $\Sigma_g(\mathbf{x}, \mathbf{x}')$ and $\Sigma_b(\mathbf{x}, \mathbf{x}')$ are the covariances for corresponding Gaussian processes. Specifically, the covariance denotes the

correlation of the values of target functions (i.e. $G[u]$ and $B[u]$) when the inputs are \mathbf{x} and \mathbf{x}' . Based on that, the NTK of a PINN, $\mathbf{K}(t)$, is defined as

$$\mathbf{K}(t) = \begin{bmatrix} \mathbf{K}_{gg}(t) & \mathbf{K}_{gb}(t) \\ \mathbf{K}_{bg}(t) & \mathbf{K}_{bb}(t) \end{bmatrix}, \quad (6)$$

where

$$\begin{aligned} (\mathbf{K}_{gg})_{ij}(t) &= \left\langle \frac{dG[u(\mathbf{x}_i^g; \boldsymbol{\theta}(t))]}{d\boldsymbol{\theta}}, \frac{dG[u(\mathbf{x}_j^g; \boldsymbol{\theta}(t))]}{d\boldsymbol{\theta}} \right\rangle, \\ (\mathbf{K}_{gb})_{ij}(t) &= \left\langle \frac{dG[u(\mathbf{x}_i^g; \boldsymbol{\theta}(t))]}{d\boldsymbol{\theta}}, \frac{dB[u(\mathbf{x}_j^b; \boldsymbol{\theta}(t))]}{d\boldsymbol{\theta}} \right\rangle, \\ (\mathbf{K}_{bb})_{ij}(t) &= \left\langle \frac{dB[u(\mathbf{x}_i^b; \boldsymbol{\theta}(t))]}{d\boldsymbol{\theta}}, \frac{dB[u(\mathbf{x}_j^b; \boldsymbol{\theta}(t))]}{d\boldsymbol{\theta}} \right\rangle. \end{aligned} \quad (7)$$

Using the NTK, training a PINN through gradient descendent algorithms can be written as

$$\begin{bmatrix} \frac{dG[u(\mathbf{x}^g; \boldsymbol{\theta}(t))]}{dt} \\ \frac{dB[u(\mathbf{x}^b; \boldsymbol{\theta}(t))]}{dt} \end{bmatrix} = -\mathbf{K}(t) \begin{bmatrix} G[u(\mathbf{x}^g; \boldsymbol{\theta}(t))] - g(\mathbf{x}^g) \\ B[u(\mathbf{x}^b; \boldsymbol{\theta}(t))] - b(\mathbf{x}^b) \end{bmatrix}. \quad (8)$$

As demonstrated by Wang et al. [51], the NTK of PINN with a sufficiently large width (i.e., $d \rightarrow \infty$) barely changes during the training process via gradient descendent algorithms

$$\mathbf{K}(0) \approx \mathbf{K}(t). \quad (9)$$

In this manner, training infinite width PINNs through a gradient descendent algorithm with enough small learning rate (also known as gradient flow [51]) can be regarded as solving a linear PDE problem, i.e.

$$\begin{bmatrix} G[u(\mathbf{x}^g; \boldsymbol{\theta}(t))] \\ B[u(\mathbf{x}^b; \boldsymbol{\theta}(t))] \end{bmatrix} \approx (\mathbf{I} - e^{-\mathbf{K}(0)t}) \begin{bmatrix} g(\mathbf{x}^g) \\ b(\mathbf{x}^b) \end{bmatrix}. \quad (10)$$

Now, consider the spectral decomposition of the NTK

$$\mathbf{K}(0) = \mathbf{Q}^T \boldsymbol{\Lambda} \mathbf{Q}, \quad (11)$$

where \mathbf{Q} is an orthogonal matrix and $\boldsymbol{\Lambda}$ is a diagonal matrix of eigenvalues. Substituting Eq. (11) into (10) leads to

$$\mathbf{Q} \begin{bmatrix} G[u(\mathbf{x}^g; \boldsymbol{\theta}(t))] - g(\mathbf{x}^g) \\ B[u(\mathbf{x}^b; \boldsymbol{\theta}(t))] - b(\mathbf{x}^b) \end{bmatrix} \approx - \begin{bmatrix} e^{-\lambda_1 t} & 0 & \dots & 0 \\ 0 & e^{-\lambda_2 t} & \dots & 0 \\ \vdots & \vdots & \ddots & \vdots \\ 0 & 0 & \dots & e^{-\lambda_n t} \end{bmatrix} \mathbf{Q} \begin{bmatrix} g(\mathbf{x}^g) \\ b(\mathbf{x}^b) \end{bmatrix}, \quad (12)$$

where λ_i denotes the i th eigenvalue and is corresponding to the convergence rate of $\mathbf{Q} \begin{bmatrix} G[u(\mathbf{x}^g; \boldsymbol{\theta}(t))] - g(\mathbf{x}^g) \\ B[u(\mathbf{x}^b; \boldsymbol{\theta}(t))] - b(\mathbf{x}^b) \end{bmatrix}$. Details regarding the proof can be found in [51].

With the aid of NTK and the corresponding NTK-based adaptive training method [51], the performance of PINN can be significantly improved for problems with high-frequency features. For example, consider a PDE and its boundary conditions as

$$\begin{aligned} \frac{d^2}{dx^2} u(x) - 4\mu^2 \pi^2 \sin(2\mu\pi x) &= 0, \quad \text{for } x \in [0, 1], \\ u(0) = u(1) &= 0, \end{aligned} \quad (13)$$

where μ is a constant that controls the frequency feature of the PDE solution. The analytical solution is given as

$$u(x) = \sin(2\mu\pi x). \quad (14)$$

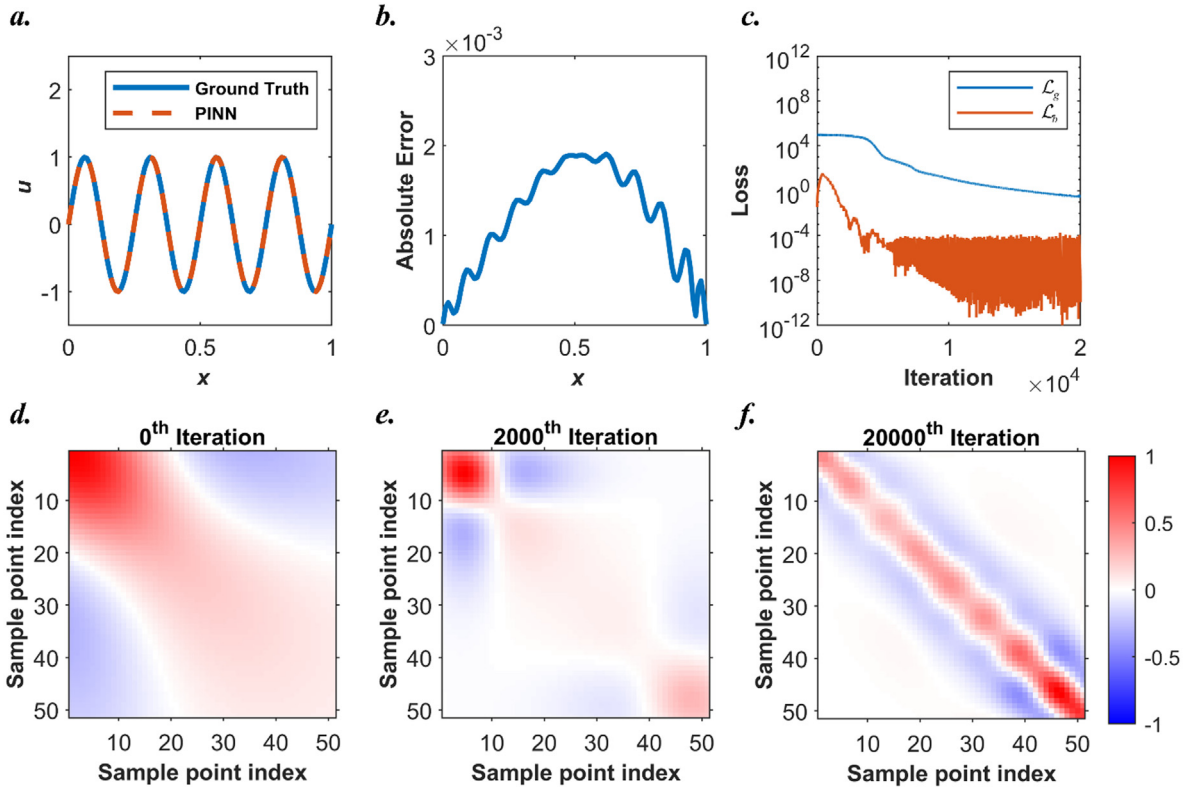


Fig. 1. Results from a PINN (single hidden layer with 61 neurons per layer) for solving Eq. (13) when $\mu = 4$. (a) Comparisons between the PINN predictions and the ground truth. (b) Point-wise absolute error plot. (c) Loss history of the PINN during the training process. (d) The normalised \mathbf{K}_g at 0th iteration. (e) The normalised \mathbf{K}_g at 2000th iteration. (f) The normalised \mathbf{K}_g at 20000th iteration.

Fig. 1 shows the predictions from PINN (one hidden layer with 61 neurons) via the NTK adaptive training methods when $\mu = 4$. Eq. (3) is used as the loss function for PINN. The tanh function is selected as the activation function and all the parameters in the PINN are initialised via the LuCun initialisation [47]. 51 sample points are uniformly distributed in the computational domain. The neural network is trained for 10^4 iterations with the Adam optimiser (learning rate 0.001). As shown in the figure, the PINN performs well for this problem and the maximum point-wise error is 1.91×10^{-3} .

Additionally, it is highlighted that the normalised NTK matrix, \mathbf{K}_g , evolves to a diagonal matrix during the training process, as shown in Fig. 1(d)–(f). This suggests that the neural network is trained to be a local approximator; that is, changing trainable parameters to approach a given data's ground truth is less likely to affect other data. The same diagonal pathology during training is observed from higher frequency cases where $\mu = 8$, as shown in Fig. 2(d)–(f). We also note that PINNs with multiple hidden layers FNNs also have this local approximation property, which are described in details in Appendix A. Nevertheless, for the higher frequency case, the FNN produce poor predictions compared to the ground truth, as shown in Fig. 2(a)(b), suggesting that a single-layer FNN with only 61 neurons is not sufficient for solving this high-frequency PDE problem. To achieve higher accuracy, a multiple hidden layers FNN is normally applied. This is because, intuitively, an FNN with an increasing number of hidden layers is more powerful in approximating a continuous function [58].

Besides, PINN also struggles to cope with problems when problem domains are ill-posed or not normalised. For example, consider Eq. (13) is translated to right by 100 to

$$\frac{d^2}{dx^2}u(x - 100) - 4\mu^2\pi^2 \sin(2\mu\pi(x - 100)) = 0, \text{ for } x \in [100, 101], \quad (15)$$

$$u(100) = u(101) = 0.$$

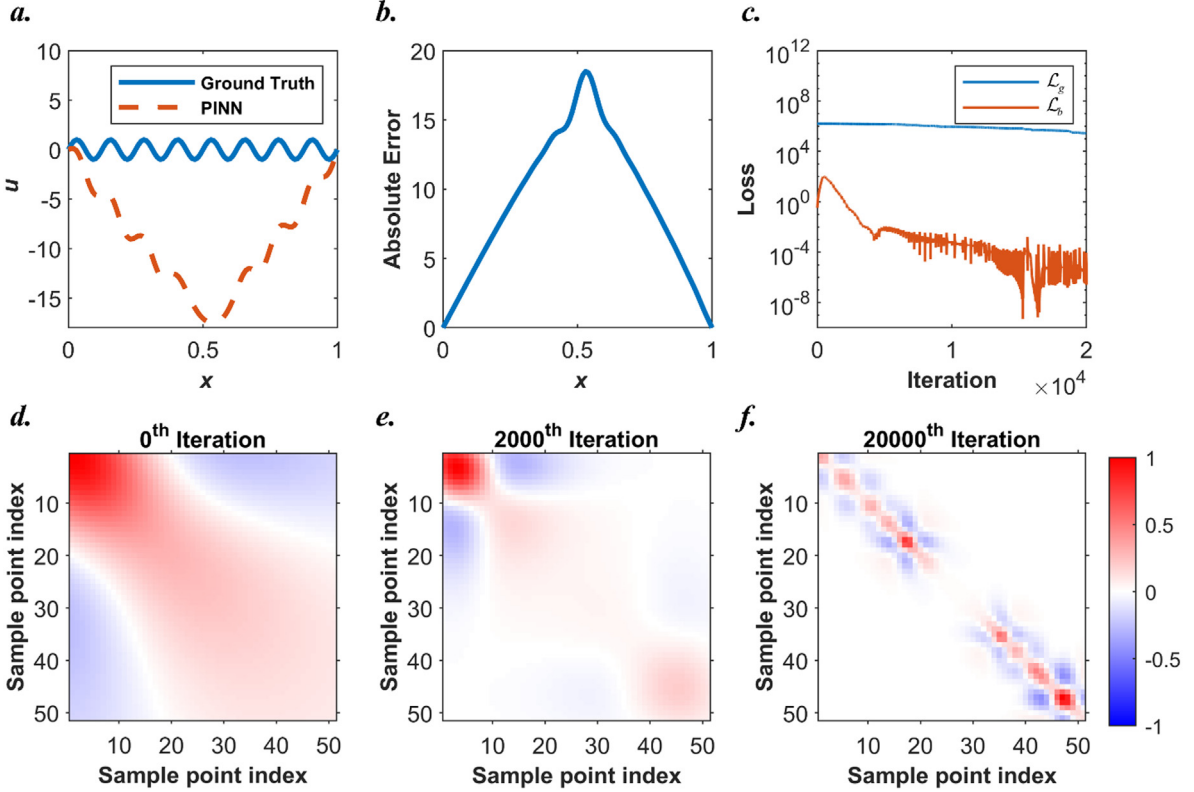


Fig. 2. Results from a PINN (single hidden layer with 61 neurons per layer) for solving Eq. (13) when $\mu = 8$. (a) Comparisons between the PINN predictions and the ground truth. (b) Point-wise absolute error plot. (c) Loss history of the PINN during the training process. (d) The normalised \mathbf{K}_g at 0th iteration. (e) The normalised \mathbf{K}_g at 2000th iteration. (f) The normalised \mathbf{K}_g at 20000th iteration.

Correspondingly, the problem domain is changed from $x \in [0, 1]$ to $x \in [100, 101]$. The PINN with the previous initialisation can suffer from severe failure, as shown in Fig. 3. It is found that all the elements of the normalised NTK of the PINN stay close to 1 from the beginning, suggesting that the sample points are highly correlated during the training process. In other words, slightly changing the trainable parameters inside the PINN can equally affect the predictions for all the sample points, which brings significant difficulties for the gradient descendent algorithm to minimise the loss. This is further demonstrated by the training plot shown in Fig. 3(c), where the loss term from the PDE, \mathcal{L}_g , almost remains at 10^4 and barely decreases along with the training.

3. Physics-informed radial basis network

As reported in Section 2, PINNs tend to be trained to a local approximator during training. For those PINNs that fail to achieve local approximation property, they can be hardly trained by physics-informed loss functions. In this manner, a question raises: will it help if a local neural network is applied? In other words, will it be more effective and efficient to train neural networks if such networks already satisfy the local approximation property before training? To answer the questions, we propose the PIRBN and test its performance.

The original radial basis network is a single-layer neural network proposed by Broomhead and Lowe [59]. In the original radial basis network, the radial basis function (RBF), $\vartheta: \mathbb{R}^n \rightarrow \mathbb{R}$, is used as the activation function. The value of an RBF depends only on the distance from a given centre, \mathbf{c} , to the input \mathbf{x} :

$$\vartheta(\mathbf{x}) = f(\|\mathbf{x} - \mathbf{c}\|), \quad (16)$$

For example, the most prevailingly used RBF in the radial basis network is the Gaussian function:

$$f(\|\mathbf{x} - \mathbf{c}\|) = e^{-b^2 \|\mathbf{x} - \mathbf{c}\|^2}, \quad (17)$$

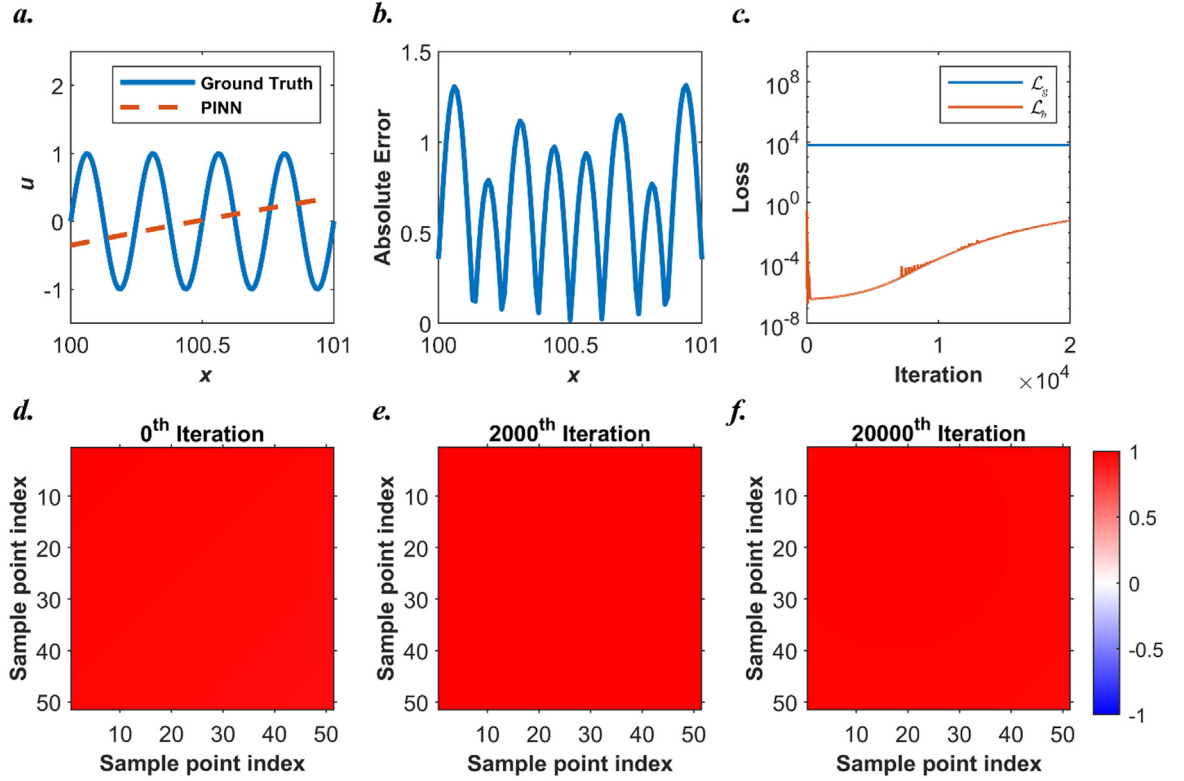


Fig. 3. Results from a PINN (single hidden layer with 61 neurons per layer) for solving Eq. (15) when $\mu = 4$. (a) Comparisons between the PINN predictions and the ground truth. (b) Point-wise absolute error plot. (c) Loss history of the PINN during the training process. (d) The normalised \mathbf{K}_g at 0th iteration. (e) The normalised \mathbf{K}_g at 2000th iteration. (f) The normalised \mathbf{K}_g at 20000th iteration.

where b is a variable that controls the shape of the RBF, as shown in Fig. 4. Besides the Gaussian function, typical RBFs also include inverse quadratic function, inverse multiquadric function, thin plate spline function, to name but a few [60]. When using the Gaussian function as the activation function, the mapping between the input and output in a radial basis network can be mathematically expressed as

$$y = \frac{1}{\sqrt{d}} \sum_i^d a_i \vartheta_i(\mathbf{x}), \quad (18)$$

where

$$\vartheta_i(x) = e^{-b_i^2 \|\mathbf{x} - \mathbf{c}_i\|^2}, \quad (19)$$

where d is the width of the radial basis network, and a_i and b_i are trainable parameters.

In this work, the radial basis network is trained with corresponding physics and its loss function can be written as Eq. (3). It is worth highlighting that, the centres of all RBF neurons of the radial basis network are constants during training, which is different from the original radial basis network. For convenience in discussion, we term this kind of radial basis network as the physics-informed radial basis network (PIRBN). An example of the PIRBN is shown in Fig. 5(a) and an original PINN is given in Fig. 5(b) for comparison.

While using PIRBNs, each RBF neuron is only activated when the input is near the centre of the neuron. Intuitively, a PIRBN exhibits the local approximation property. In what follows, the NTK theory is applied to study the training dynamics of PIRBN and therefore proves the local approximation property of PIRBN during training. Furthermore, corresponding initialisation strategies are also presented and discussed in detail.

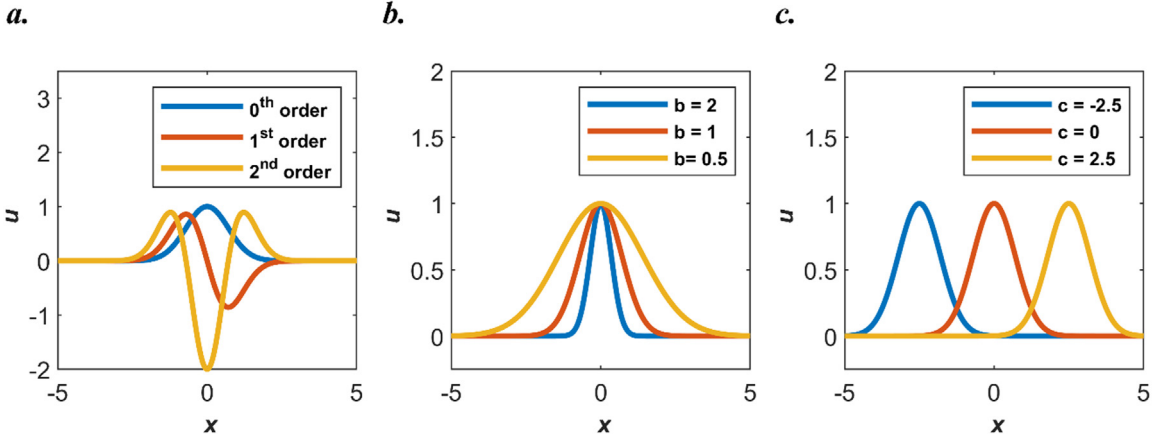


Fig. 4. An example of the Gaussian function. (a) 0th, 1st and 2nd orders derivatives of the Gaussian function. (b) The Gaussian function with different b . (c) The Gaussian function with different c .

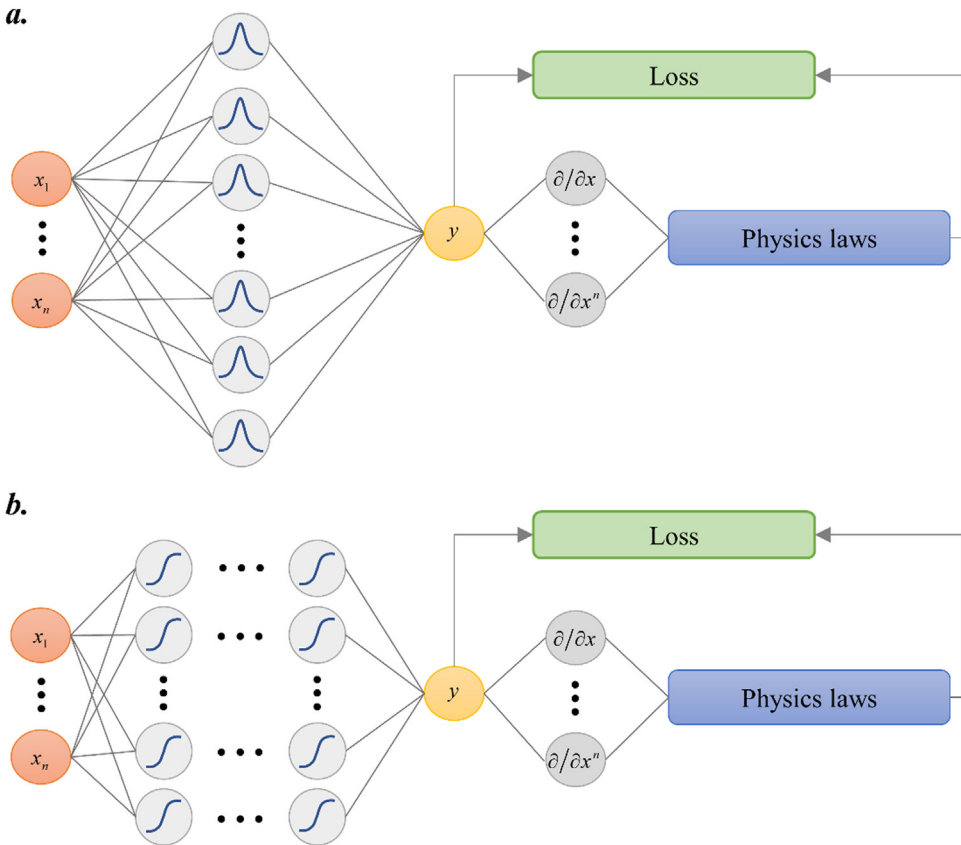


Fig. 5. (a) The structure of a physics-informed radial basis network (PIRBN). (b) The structure of a physics-informed neural network (PINN).

3.1. Analysing PIRBN via the NTK theory

As aforementioned, the NTK theory provides a powerful tool to investigate the training process of PINNs. The training process of a PIRBN via gradient descendent algorithms can also be analysed by the NTK theory, which is presented here.

As an example, consider the problem defined by Eq. (15), for which we had difficulty training a PINN. A PIRBN with the Gaussian function is now constructed to solve this problem. The Adam optimiser is also used. Before analysis, the parameters a_i in the PIRBN are initialised with i.i.d. random variables satisfy $\mathcal{N}(0, 1)$ distribution and c_i are initialised as constants so that the RBF neurons can be uniformly distributed in the computational domain. Besides, b_i in the PIRBN are initialised to a given value. These are important prerequisites to obtaining the following theorems.

Theorem 3.1.1. *As $d \rightarrow \infty$, an initialised PIRBN predictions converge to centred Gaussian processes*

$$\begin{aligned} \lim_{d \rightarrow \infty} \frac{d^2}{dx^2} u(\mathbf{x}; \boldsymbol{\theta}(t)) &\rightarrow \mathcal{GP}(0, \Sigma_g(\mathbf{x}, \mathbf{x}')), \\ \lim_{d \rightarrow \infty} u(\mathbf{x}; \boldsymbol{\theta}(t)) &\rightarrow \mathcal{GP}(0, \Sigma_b(\mathbf{x}, \mathbf{x}')), \end{aligned} \quad (20)$$

where $\Sigma_g(x, x')$ and $\Sigma_b(x, x')$ are their corresponding covariances

$$\begin{aligned} \Sigma_g(\mathbf{x}, \mathbf{x}') &= \mathbb{E}[a^2 \ddot{\vartheta}(\mathbf{x}) \ddot{\vartheta}(\mathbf{x}')], \\ \Sigma_b(\mathbf{x}, \mathbf{x}') &= \mathbb{E}[\vartheta(\mathbf{x}) \vartheta(\mathbf{x}')]. \end{aligned} \quad (21)$$

Proof. The proof of this theorem is given in [Appendix B.1](#).

Remark 3.1.2. [Theorem 3.1.1](#) indicates that, as $d \rightarrow \infty$, the training process of a PIRBN can be regarded as Gaussian processes [47]. In other words, training a PIRBN via gradient descendent algorithms can also be regarded as a kernel-based regression problem [61]. Therefore, based on [Theorem 3.1.1](#) and followed by the definition of the NTK for a PINN, we can also define the NTK of a PIRBN as Eqs. (6) and (7). It is worth noting that, the NTK of a PIRBN is the covariance matrix for the Gaussian processes. That is, each element in the NTK, K_{ij} , indicate the covariance between two inputs x_i and x_j . Meanwhile, the NTK of a PIRBN suffices the following properties:

Theorem 3.1.3. *As $d \rightarrow \infty$, the NTK of PIRPN at the initialisation converges to a deterministic kernel \mathbf{K}'*

$$\lim_{d \rightarrow \infty} \mathbf{K}(0) \rightarrow \mathbf{K}'. \quad (22)$$

Proof. The proof is given in [Appendix B.2](#).

Theorem 3.1.4. *As $d \rightarrow \infty$, assume that there exists a constant \mathcal{C} such that*

$$\begin{aligned} \sup_{t \in [0, T]} \|\mathbf{a}(t)\|_\infty &\leq \mathcal{C}, \\ \sup_{t \in [0, T]} \|\mathbf{b}(t)\|_\infty &\leq \mathcal{C}, \\ \int_0^T \left| \sum_i^{n_g} (\mathbf{G}[u(x_i^g, \boldsymbol{\theta}(\sigma))] - g(x_i^g)) \right| d\sigma &\leq \mathcal{C}, \\ \int_0^T \left| \sum_i^{n_b} (\mathbf{B}[u(x_i^b, \boldsymbol{\theta}(\sigma))] - b(x_i^b)) \right| d\sigma &\leq \mathcal{C}, \end{aligned}$$

during the training process, i.e. $t \in [0, T]$. Then, the NTK of PIRBN through the gradient descendent algorithm suffices

$$\lim_{d \rightarrow \infty} \sup_{t \in [0, T]} \|\mathbf{K}(t) - \mathbf{K}(0)\|_2 = 0. \quad (23)$$

Proof. The proof is given in [Appendix B.3](#).

Remark 3.1.5. Based on the above Theorems, as $d \rightarrow \infty$, one can conclude that the NTK of a PIRBN remains unchanged during the training of the PIRBN via gradient descendent algorithms. In fact, when the width of a PIRBN

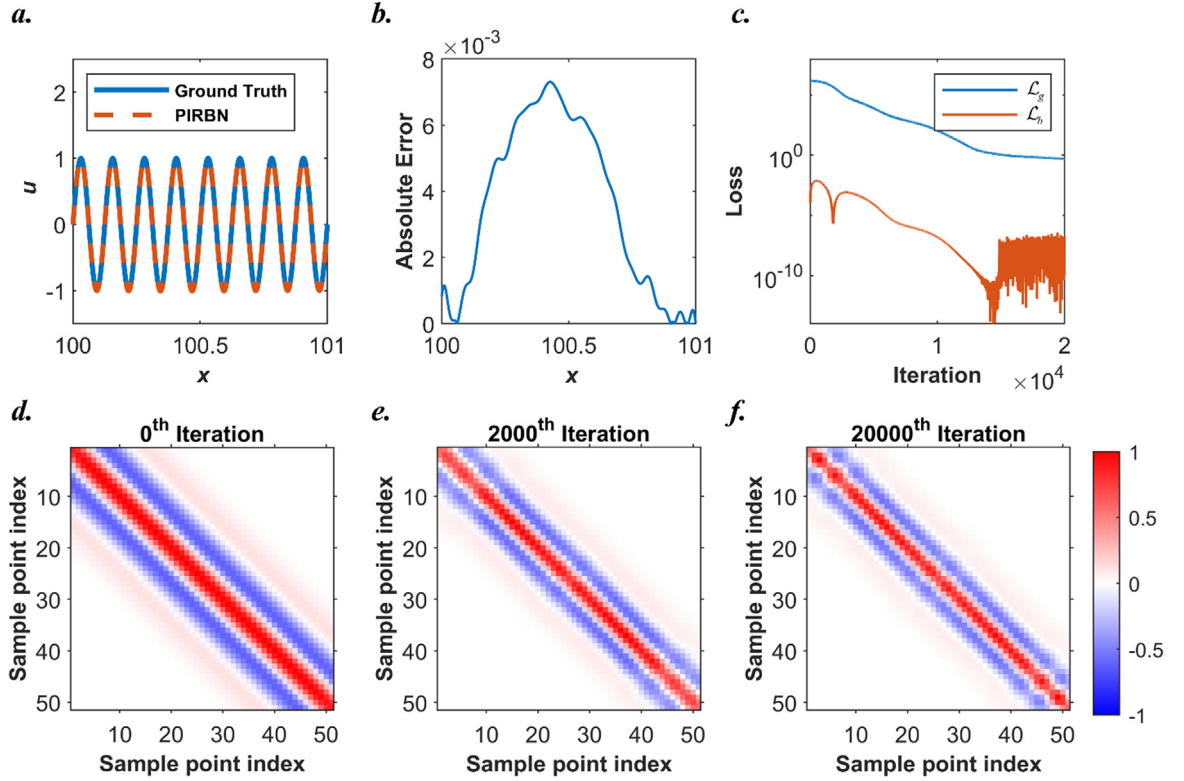


Fig. 6. Results from a PIRBN (single hidden layer with 61 neurons per layer) for solving Eq. (15) when $\mu = 8$. (a) Comparisons between the PIRBN predictions and the ground truth. (b) Point-wise absolute error plot. (c) Loss history of the PIRBN during the training process. (d) The normalised \mathbf{K}_g at 0th iteration; (e) The normalised \mathbf{K}_g at 2000th iteration; (f) The normalised \mathbf{K}_g at 20000th iteration.

is enough large, the NTK of the PIRBN also approximately remains static during training. Hence, training a PIRBN with enough large width through gradient descendent algorithms can also be regarded as solving a linear PDE problem, as stated in Eq. (10). Meanwhile, the NTK-based adaptive training scheme proposed by Wang et al. [51] is applicable for PIRBN with gradient descendent training algorithms.

By using the PIRBN with the NTK-based adaptive training scheme, we recall the problem Eq. (15) with $\mu = 8$. A PIRBN is set up with also 61 neurons. The centres of PIRBN neurons are uniformly distributed within [99.9, 101.1] and initial $b = 10$. Fig. 6 shows the results from PIRBN after 2×10^4 iterations via Adam optimiser (learning rate 0.001). The prediction obtained from the PIRBN aligns well with the analytical solution. Besides, the maximum point-wise absolute error is 7.31×10^{-3} . The loss terms converge after 1.5×10^4 iterations. Additionally, it is clear to find that the normalised NTK of the PIRBN remains as a diagonal matrix at the initial stage (0th iteration), 2000th iteration and 20000th iteration, suggesting that the PIRBN exhibits a well-local approximation property throughout the whole training process.

3.2. Parameter initialisation

In this part, we discuss the parameter initialisation for a PIRBN. For the sake of simplicity, the 1D PDE problem state in Eq. (15) is used as an example and the Gaussian function is selected for the PIRBN. As mentioned in the previous section, to analyse the training process of PIRBN via the NTK theory, weights in the second layer, a_i , require to be initialised as i.i.d. $\mathcal{N}(0, 1)$ variables. Therefore, we only discuss the initialisation schemes for PIRBN with respect to b_i and c_i .

We first start with the parameter b . As aforementioned, b controls the width of the Gaussian function. Given that the Gaussian function has the following property

$$\frac{\int_{-3/|b|}^{3/|b|} \vartheta(x)dx}{\int_{-\infty}^{+\infty} \vartheta(x)dx} \approx 99.8\%, \quad (24)$$

we define the impact area of a Gaussian function neuron as $[c - 3/|b|, c + 3/|b|]$. Thus, for 1D uniformly distributed sample points, the number of sample points within a Gaussian function, δ , can be calculated as

$$\delta = 2 \left\lfloor \frac{3}{|b| \cdot dx} \right\rfloor + 1, \quad (25)$$

where dx denotes the sample points spacing. δ can greatly influence the convergence rate of PIRBN's training process and the accuracy of PIRBN's prediction. Examples of PIRBNs initialised with different b are presented in Fig. 7. It is observed that, with a smaller initial b , the NTK of the PIRBN exhibits poor diagonal property, suggesting that sample points inside the computational domain are still highly coupled with each other during the training process. On the contrary, with decreasing initial b , the NTK of the PIRBN exhibits a better diagonal property. However, too large initial b can induce insufficient sample points within the impact area of a Gaussian function neuron. In this case, the PIRBN will fail to govern the area between sample points, resulting in low accuracy when solving PDEs. This can be further demonstrated by Fig. 8, which presents histories of loss and mean absolute error (MAE) of PIRBNs with different initialised b for solving Eq. (15). With increasing b , the loss and MAE of PIRBNs converge faster. However, despite the fastest convergence rate of loss shown in Fig. 8(a) when b is initialised as 100, the MAE of the PIRBN shown in Fig. 8(b) does not decrease and remains at a high level during the training process. Meanwhile, the loss of the PIRBN with initial $b = 100$ jumps up after 1×10^4 iterations. This is because, as shown in Fig. 4, a too large initial value of b will minimise the activated area of a radial basis neuron. Therefore, by initialising $b = 100$, there are only limited overlapping areas between any two neurons. Fig. 9 shows the comparison between PIRBNs with initial $b = 100$ and $b = 25$. During the training of such a neural network, each neuron is activated by an insufficient number of sample points. In other words, the neurons in such a network are decoupled with each other. Consequently, the optimiser only modifies the neuron based on the loss obtained from the insufficient sample point that activates this neuron, while ignoring the correlations between adjacent neurons. Thus, the loss of the PIRBN will quickly reach a very low level. These numerical experiments indicate that one should at least make sure that the RBF neurons with the selected initial b can cover a sufficient number of sample points in the computational domain when using PIRBNs. Besides, the RBF neurons with the selected initial b should have some overlapping area with the adjacent RBF neurons. As for this numerical case, $b = 25$ is suggested from accuracy and efficiency regards.

Next, we discuss the initialisation for the centre of each RBF neuron. As aforementioned, c controls the location of the centre of an RBF neuron. Given that the computational domain for most PINN applications is bounded, most of the centres of RBF neurons in a PIRBN should be initialised inside the computational domain. Specifically, extra Gaussian function neurons whose centres are around the outer edge of the boundaries are required, as shown in Fig. 10(a). By adding those outer edge RBF neurons, PIRBN has an increasing capability of approximating the boundary conditions. Compared to PIRBN without the outer edge neurons shown in Fig. 10(b), the \mathcal{L}_b of the PIRBN with outer edge neurons can converge faster and reach a lower level, as shown in Fig. 10(c). Based on our numerical experimental experiences, 4–10 outer edge neurons are suggested.

Till now, only PIRBNs with uniformly distributed Gaussian function neurons are considered within the computational domain. We further test the performance of PIRBNs when using randomly distributed Gaussian function neurons. The initial b for all cases is set to be 10 so that δ for all cases is no less than 15. Fig. 11 shows the results from PIRBNs by using uniformly and randomly distributed Gaussian function neurons. Compared with the PIRBN with uniformly distributed centres, the PIRBN with randomly distributed centres exhibits poor performance. The maximum point-wise absolute error produced by PIRBN with randomly distributed centres is 0.011, while the maximum point-wise absolute error produced by PIRBN with uniformly distributed centres is 0.007. Table 1 lists the mean values of \mathcal{L}_g , \mathcal{L}_b and MAE by using PIRBNs with randomly and uniformly distributed centres. As observed, both losses and MAE of the PIRBN with uniformly distributed centres reach significantly lower levels than the PIRBN with randomly distributed centres, suggesting that the randomly distributed centres significantly influence the performance of the PIRBN. In this manner, uniformly distributed Gaussian function neurons are suggested

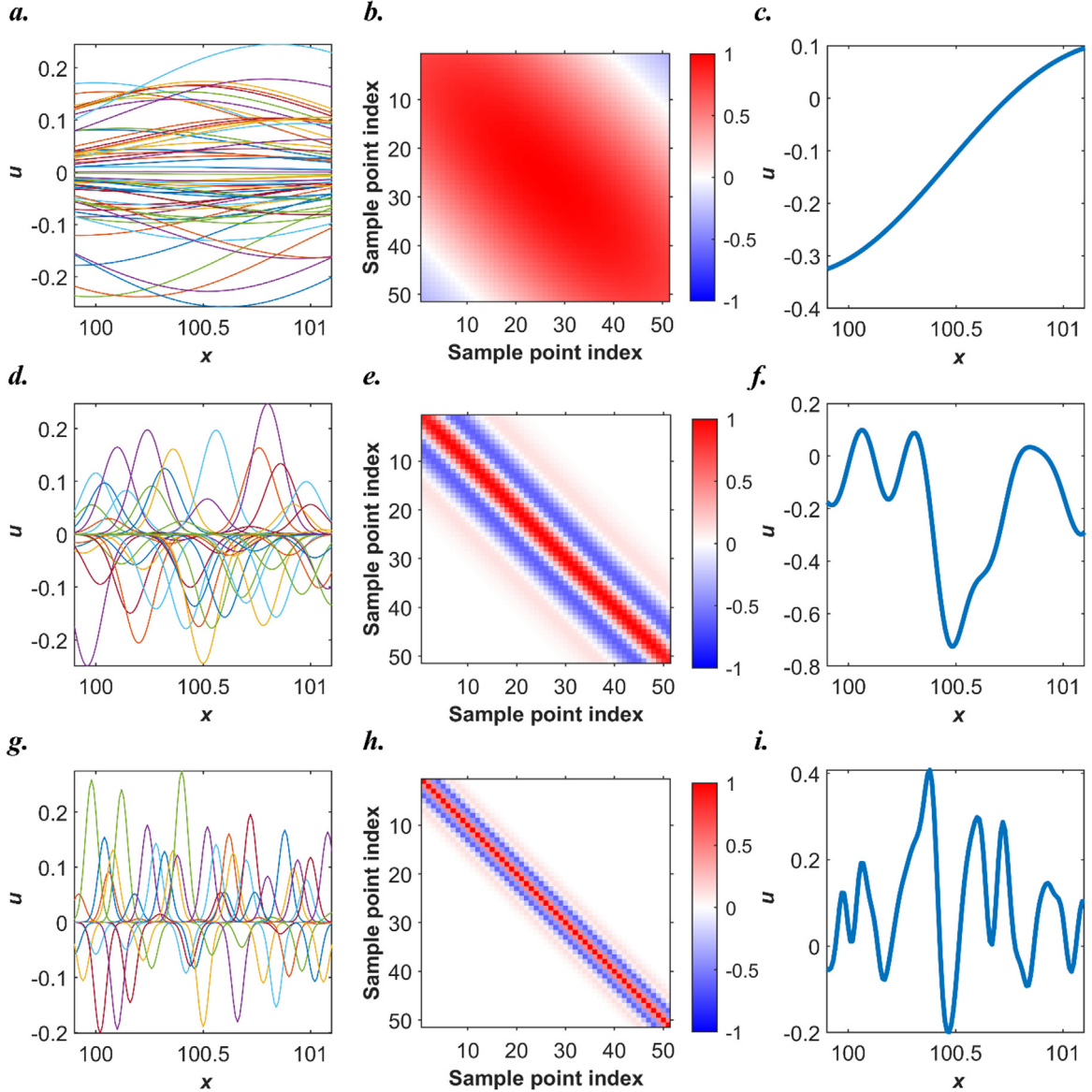


Fig. 7. Initialise a PIRBN with different b . Centres of RBF neurons are uniformly distributed within [99.9, 101.1]. (a) All Gaussian function neurons plot when initial $b = 1$. (b) The normalised \mathbf{K}_g at the initial stage when initial $b = 1$. (c) The prediction of the PIRBN at the initial stage when initial $b = 1$. (d) All Gaussian function neurons plot when initial $b = 10$. (e) The normalised \mathbf{K}_g at the initial stage when initial $b = 10$. (f) The prediction of the PIRBN at the initial stage when initial $b = 10$. (g) All Gaussian function neurons plot when initial $b = 25$. (h) The normalised \mathbf{K}_g at the initial stage when initial $b = 25$. (i) The prediction of the PIRBN at the initial stage when initial $b = 25$.

for this problem. However, we note that a number of adaptive sampling strategies have been proposed [62,63], which can significantly improve the performance of physics-informed deep learning. More investigations regarding integrating adaptive sampling strategies with the proposed PIRBN are encouraged.

3.3. Number of sample points

To test the performance of PIRBN with different sample points inside the computational domain, 5 different numbers of uniformly distributed sample points are used to solve Eq. (15). For all cases, 601 Gaussian function

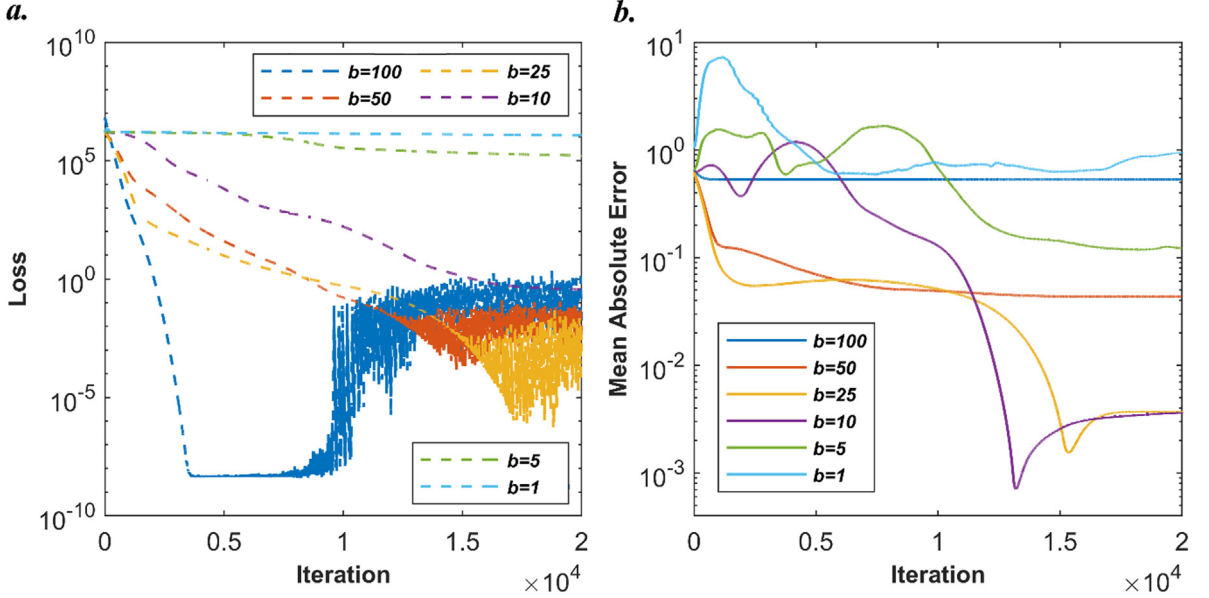


Fig. 8. (a) Loss history of PIRBNs initialised with different initial b . (b) Mean absolute error history of PIRBNs with different initial b .

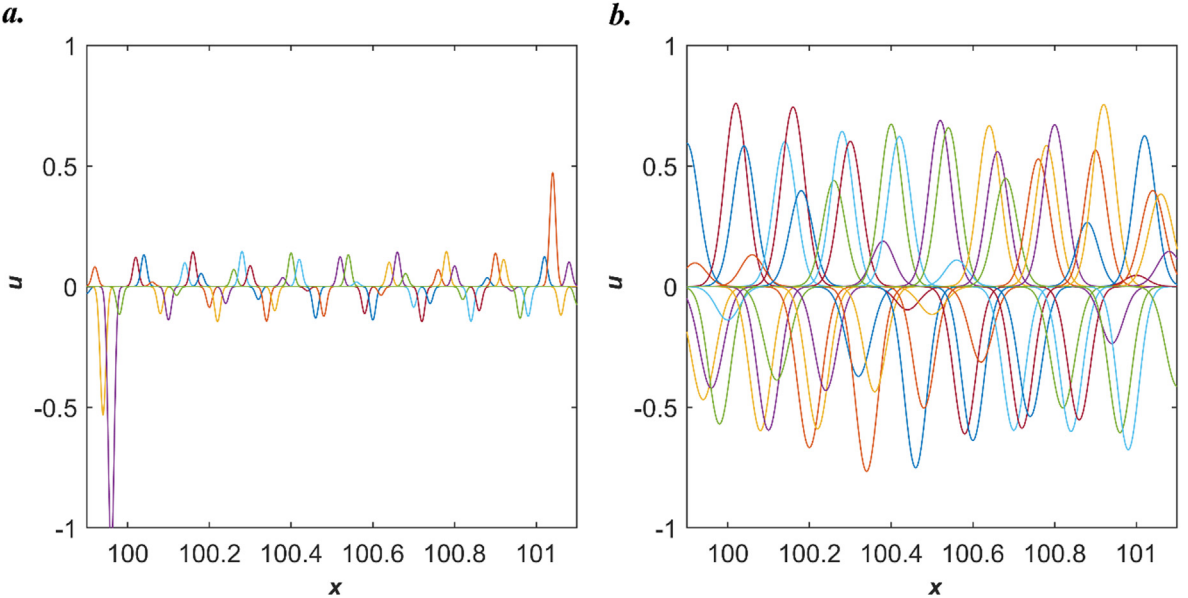


Fig. 9. RBF neurons plot of PIRBNs after training. (a) Initial $b = 100$; (b) Initial $b = 25$.

Table 1

Comparisons of \mathcal{L}_g , \mathcal{L}_b and mean absolute error between PIRBNs with randomly and uniformly distributed centres. Initial b is set to be 10. The values are obtained from 20 times runs.

	\mathcal{L}_g	\mathcal{L}_b	Mean absolute error (MAE)
Random	23.99 ± 32.31	$2.21 \pm 3.96 \times 10^{-3}$	$7.55 \pm 7.10 \times 10^{-3}$
Uniform	0.46 ± 0.14	$4.51 \pm 8.24 \times 10^{-9}$	$3.62 \pm 0.12 \times 10^{-3}$

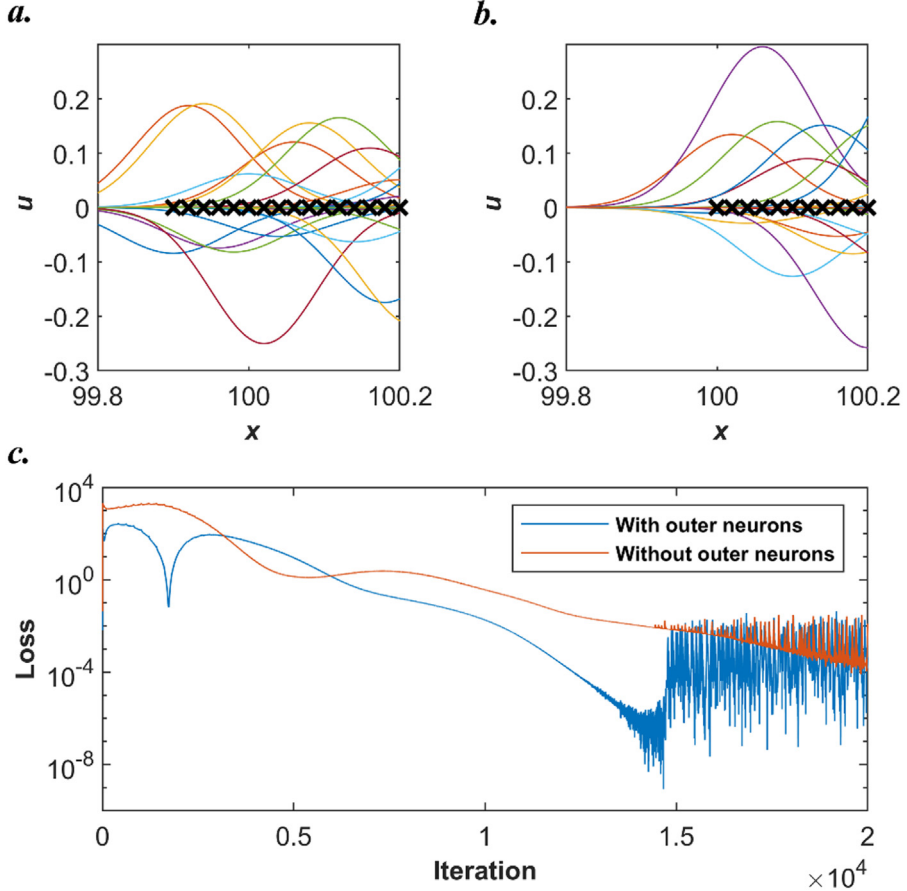


Fig. 10. (a) Initialise PIRBN with extra Gaussian function neurons at the outer edge of the computational domain. (b) Initialise PIRBN without extra Gaussian function neurons at the outer edge of the computational domain. The black crosses denote the centres of the Gaussian function neurons. (c) Loss history of \mathcal{L}_b during the training process.

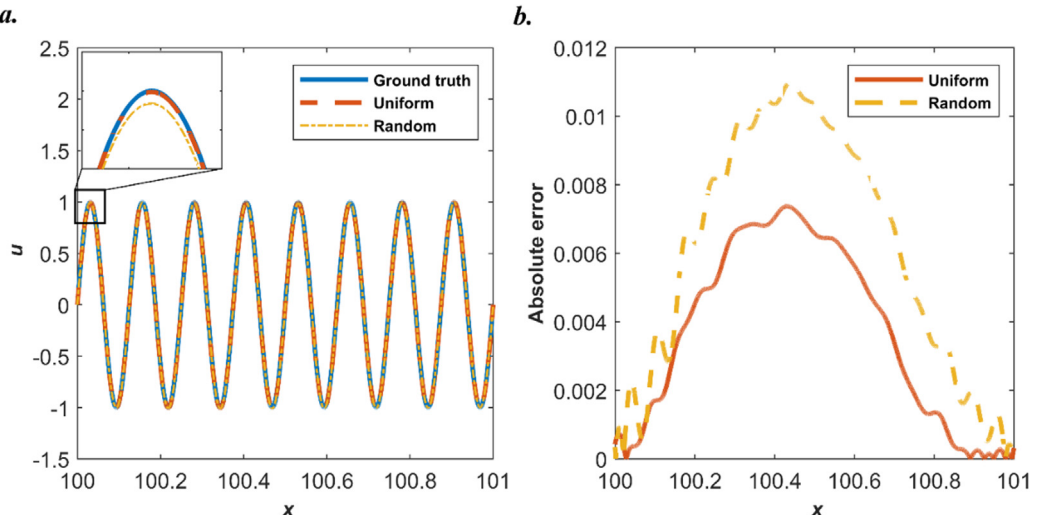


Fig. 11. Results from PIRBNs by using uniformly and randomly distributed Gaussian function neurons. (a) Comparisons between the analytical solution and predictions from PIRBNs by using uniformly and randomly distributed Gaussian function neurons. (b) The point-wise absolute error of predictions from PIRBNs.

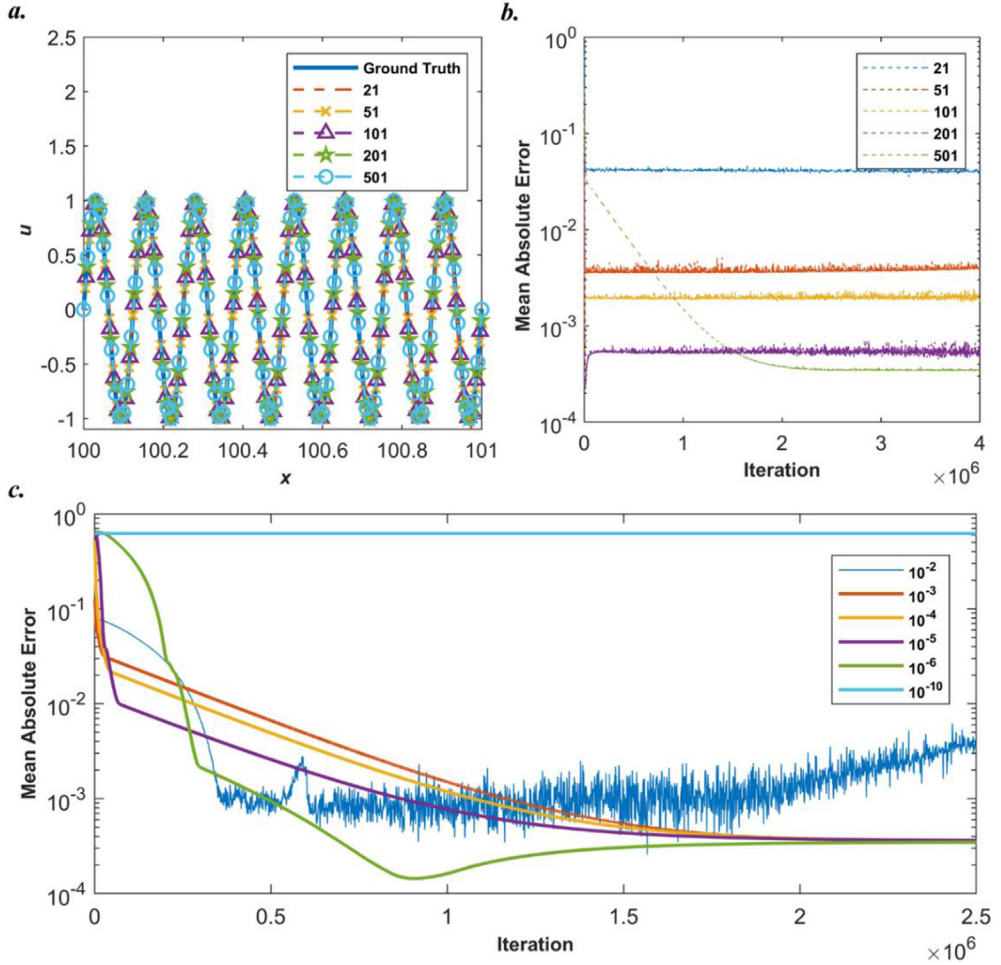


Fig. 12. Results from PIRBNs by using different numbers of uniformly distributed sample points. (a) Comparisons between the analytical solution and predictions from PIRBNs with different numbers of uniformly distributed sample points. (b) MAE history of PIRBNs with different numbers of sample points throughout training processes. (c) Convergence plots for PIRBN training with learning rates as 10^{-2} , 10^{-3} , 10^{-4} , 10^{-5} , 10^{-6} and 10^{-10} .

neurons are uniformly distributed within $[99.9, 101.1]$. Different initial b values are set for different cases so that $\delta \approx 21$ for all cases.

Fig. 12 compares the results from PIRBN with different numbers of uniformly distributed sample points. As shown in Fig. 12(a), the predictions from PIRBNs with different numbers of sample points agree well with the analytical solution, suggesting that all the cases can effectively solve the problem. Fig. 12(b) shows the MAE history of PIRBNs with different numbers of sample points throughout the training processes. As observed, the accuracy of PIRBN can be increased with the increasing number of sample points. However, it is also found that, with the same learning rate, using more sample points requires more iterations for convergence. Considering that more sample points can make the PIRBN training more sensitive, too large a learning rate may be difficult for convergence. We further test the influence of the learning rate for PIRBN training, and the convergence plot is presented in Fig. 12(c). The learning rates of the six plots are 10^{-2} , 10^{-3} , 10^{-4} , 10^{-5} , 10^{-6} and 10^{-10} . As observed, when using the learning rate 10^{-2} , the training of the PIRBN is unstable and fails to converge. When the learning rate is smaller than 10^{-2} , the training of a PIRBN can converge earlier with the decreasing learning rate till 10^{-6} . Nevertheless, applying too small a learning rate can lead to slower convergence, as the convergence plot for 10^{-10} . Hence, the selection of a proper learning rate can enhance PIRBNs' training efficiency.

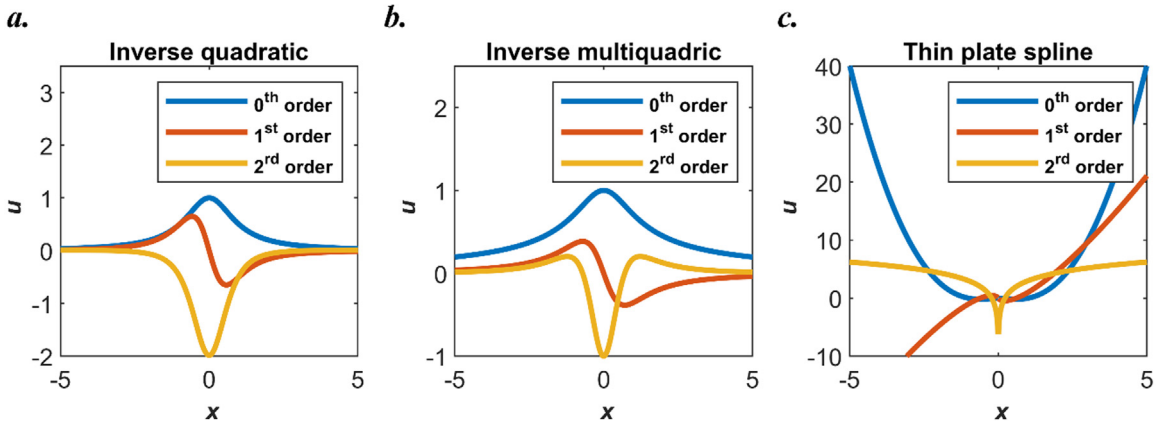


Fig. 13. Illustrations of some typical RBFs. (a) The inverse quadratic function; (b) The inverse multiquadric function; (c) The thin plate spline.

3.4. Selection of RBF

As previously mentioned, there are various types of RBF. However, not all types of RBF are effective for constructing a PIRBN. Considering the prerequisites in the theorems, the RBF used in PIRBN should satisfy the following requirements:

- (i) The selected RBF should be high-order differentiable (infinitely smooth).
- (ii) The selected RBF and its derivatives should be bounded.
- (iii) The selected RBF should have a local impact.

Herein, we choose four typical RBFs and test performances of PIRBN with different RBFs, including the Gaussian function, the inverse quadratic function, the inverse multiquadric function and the thin plate spline, as shown in Fig. 13. Apart from the Gaussian function, the following expressions of the rest RBFs are provided as

$$\text{Inverse quadratic function: } R_{\text{iq}}(\|\mathbf{x} - \mathbf{c}\|) = \frac{1}{1 + b^2 \|\mathbf{x} - \mathbf{c}\|^2}, \quad (26)$$

$$\text{Inverse multiquadric function: } R_{\text{imq}}(\|\mathbf{x} - \mathbf{c}\|) = \frac{1}{\sqrt{1 + b^2 \|\mathbf{x} - \mathbf{c}\|^2}}, \quad (27)$$

$$\text{Thin plate spline: } R_{\text{tp}}(\|\mathbf{x} - \mathbf{c}\|) = b^2 \|\mathbf{x} - \mathbf{c}\|^2 \ln(\sqrt{b^2 \|\mathbf{x} - \mathbf{c}\|^2 + 1}). \quad (28)$$

It is clear that only the thin plate spline does not fully satisfy the requirements, for the thin plate spline and its derivatives are neither bounded nor have local impact.

Now, consider a PDE and its boundary conditions

$$\frac{d^2}{dx^2} u(x) = f(x), \text{ for } x \in [20, 22], \quad (29)$$

$$u(20) = u(22) = 0,$$

where $f(x)$ is a tailored function so that the solution of this PDE can be written as

$$u(x) = \left(\frac{22-x}{2}\right)^2 \sin(2\pi x) + \left(\frac{x-20}{2}\right)^2 \sin(16\pi x). \quad (30)$$

Again, this problem is challenging for PINN since the computational domain is not normalised. Besides, the analytical solution contains both low-frequency and high-frequency features; that is, the solution exhibits a low-frequency feature when x is closer to 20, while the solution exhibits a high-frequency feature when x is approaching 22. Fig. 14 shows the results obtained by using PINN (one hidden layer and 121 neurons in the hidden layer). As

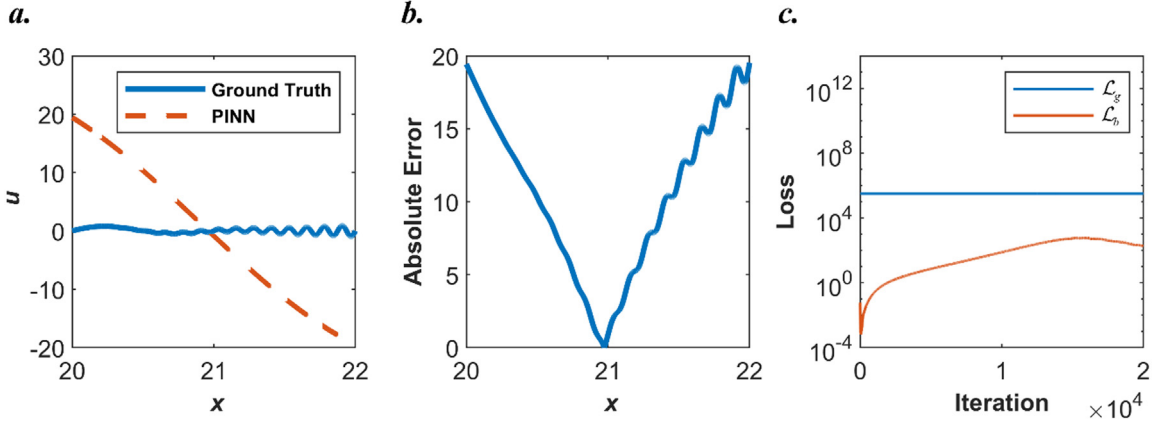


Fig. 14. Results from a PINN (single hidden layer with 61 neurons per layer) for solving Eq. (29). (a) Comparisons between the predictions from the PINN and the analytical solution. (b) Point-wise absolute error from the PINN. (c) Loss history of the PINN during the training process.

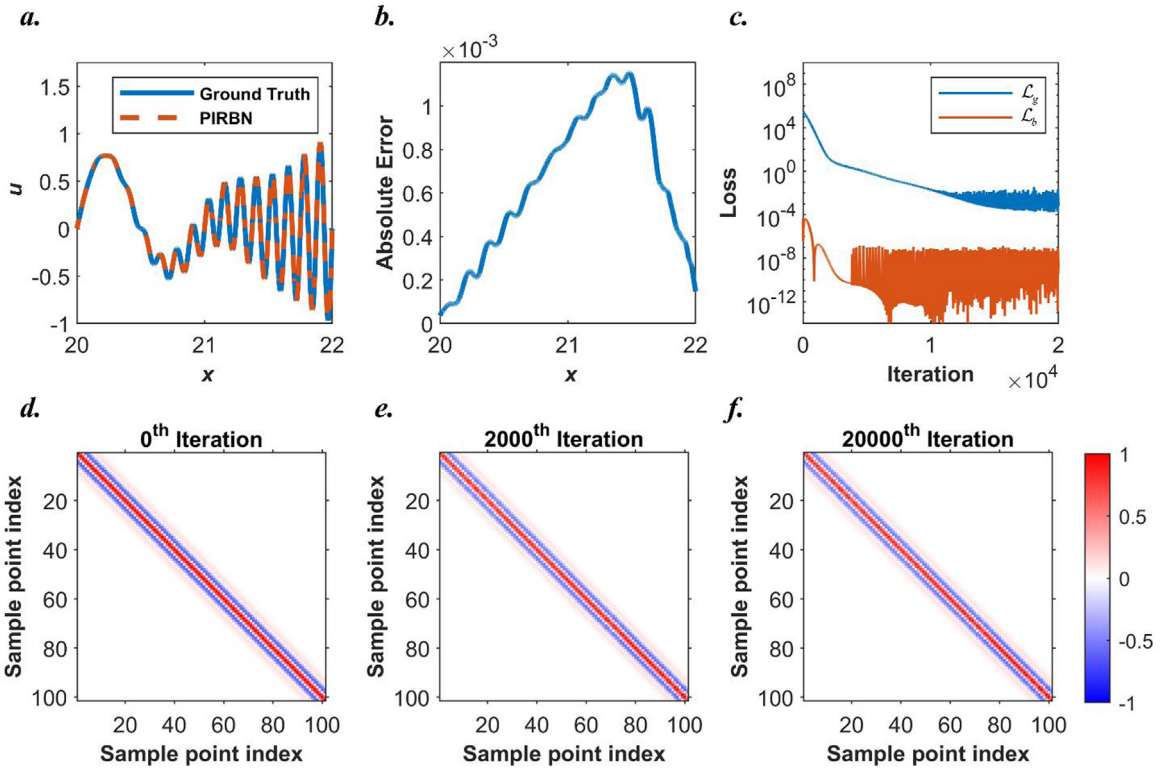


Fig. 15. Results from a PIRBN (single hidden layer with 101 neurons per layer) with the Gaussian function for solving Eq. (29). (a) Comparisons between the predictions from the PIRBN and the analytical solution. (b) Point-wise absolute error from the PIRBN. (c) Loss history of the PIRBN during the training process. (d) The normalised \mathbf{K}_g at the 0th iteration. (e) The normalised \mathbf{K}_g at the 2000th iteration; (f) The normalised \mathbf{K}_g at the 20000th iteration.

observed, PINN fails to solve this problem by using the Adam optimiser (learning rate 0.001) after 2×10^4 iterations. The loss terms from the PDE can be hardly decreased during the training process, as shown in Fig. 14(c).

Figs. 15–17 show the results obtained by using PIRBNs (121 uniformly distributed neurons) with the Gaussian function, the inverse quadratic function and the inverse multiquadric function, respectively. All these PIRBNs can

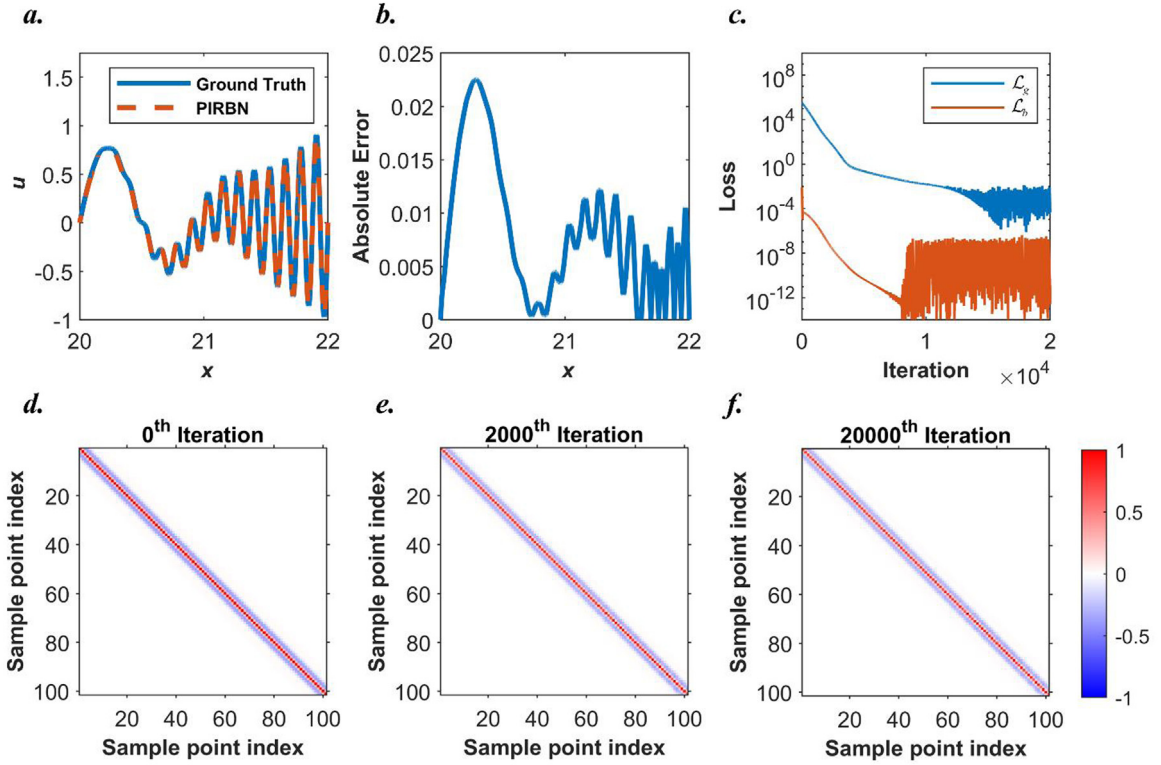


Fig. 16. Results from a PIRBN (single hidden layer with 101 neurons per layer) with the inverse quadratic function for solving Eq. (29). (a) Comparisons between the predictions from the PIRBN and the analytical solution. (b) Point-wise absolute error from the PIRBN. (c) Loss history of the PIRBN during the training process. (d) The normalised \mathbf{K}_g at the 0th iteration. (e) The normalised \mathbf{K}_g at the 2000th iteration; (f) The normalised \mathbf{K}_g at the 20000th iteration.

effectively solve the problem with good accuracy via the Adam optimiser after 2×10^4 iterations. Besides, NTKs for all these PIRBNs retain as diagonal matrixes throughout the training processes, as shown in Figs. 15(d)–(f), 16(d)–(f) and 17(d)–(f). Among them, the PIRNB with the Gaussian function performs the best, while the largest point-wise absolute error is 1.15×10^{-3} .

Fig. 18 shows the results obtained by using a PIRBN with the thin plate spline. As observed from Fig. 18(a) and (b), the PIRBN fails to solve the problem, suggesting that not all RBFs can be effective for constructing a PIRBN. In terms of the loss history of the PIRBN with the thin plate spline plotted in Fig. 18(c), all loss terms remain at a high level during the training process, suggesting that the PIRBN with the thin plate spline cannot be well-trained. This is further proved by the MAE plot which remains nearly unchanged throughout the whole training process, as also shown in Fig. 18(c).

4. Numerical examples

In this section, several numerical examples are conducted to demonstrate the performance of PIRBN towards different PDEs. All those PDEs are prevailingly used in various applications. We note that all examples are trained on a Windows 10 system with Intel(R) Core(TM) i7-8700 CPU@3.20 GHz. The neural networks are built based on the TensorFlow library. The Adam optimiser is selected as the training algorithm. The programs that can regenerate all numerical results can be found at <https://github.com/JinshuaiBai/PIRBN>.

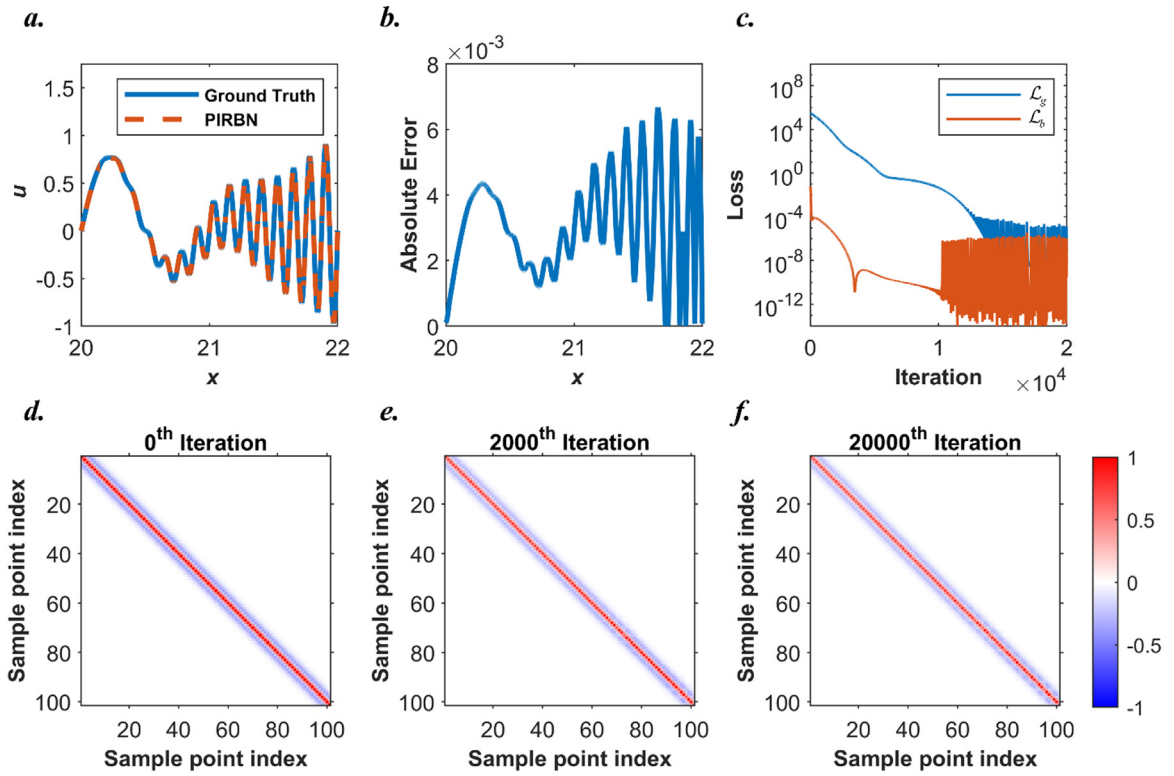


Fig. 17. Results from a PIRBN (single hidden layer with 101 neurons per layer) with the inverse multiquadric function for solving Eq. (29). (a) Comparisons between the predictions from the PIRBN and the analytical solution. (b) Point-wise absolute error from the PIRBN. (c) Loss history of the PIRBN during the training process. (d) The normalised \mathbf{K}_g at the 0th iteration. (e) The normalised \mathbf{K}_g at the 2000th iteration; (f) The normalised \mathbf{K}_g at the 20000th iteration.

4.1. 1D nonlinear spring equation

Consider a 1D nonlinear spring equation with the following initial and boundary conditions:

$$\begin{aligned} \frac{d^2}{dx^2}u(x) + 4u(x) + \sin(u(x)) &= f(x), \quad \text{for } x \in [0, 100], \\ u(0) &= 0 \\ \frac{d}{dx}u(0) &= 0 \end{aligned} \tag{31}$$

where $f(x)$ is a tailored function so that the analytical solution of this problem can be written as

$$u(x) = x \sin(x). \tag{32}$$

This problem is quite challenging for PINN due to the existances of a long-range computational domain $x \in [0, 100]$, large predict value and high-frequency feature. To address this problem via PINN, Dong and Li [43] decomposed the whole computational domain into pieces and applied multiple neural networks to approximate the solution for each subdomain. Here, we apply a PIRBN with 1021 neurons to solve this problem. The centres of neurons are uniformly distributed within $[1, 101]$, and the initial b is set to 10. Besides, a PINN with the same number of hidden layer and neurons is also applied for comparison.

Fig. 19 compares the results from PINN and PIRBN for solving the 1D nonlinear spring equation, respectively. As observed from Fig. 19(a) and (b), the predictions from the PIRBN align well with the analytical solution, while the largest point-wise absolute error is 8×10^{-3} . On the contrary, the prediction from PINN only aligns the analytical results at the area close to $x = 0$, as shown in Fig. 19(d) and (e). Meanwhile, the loss terms from PIRBN

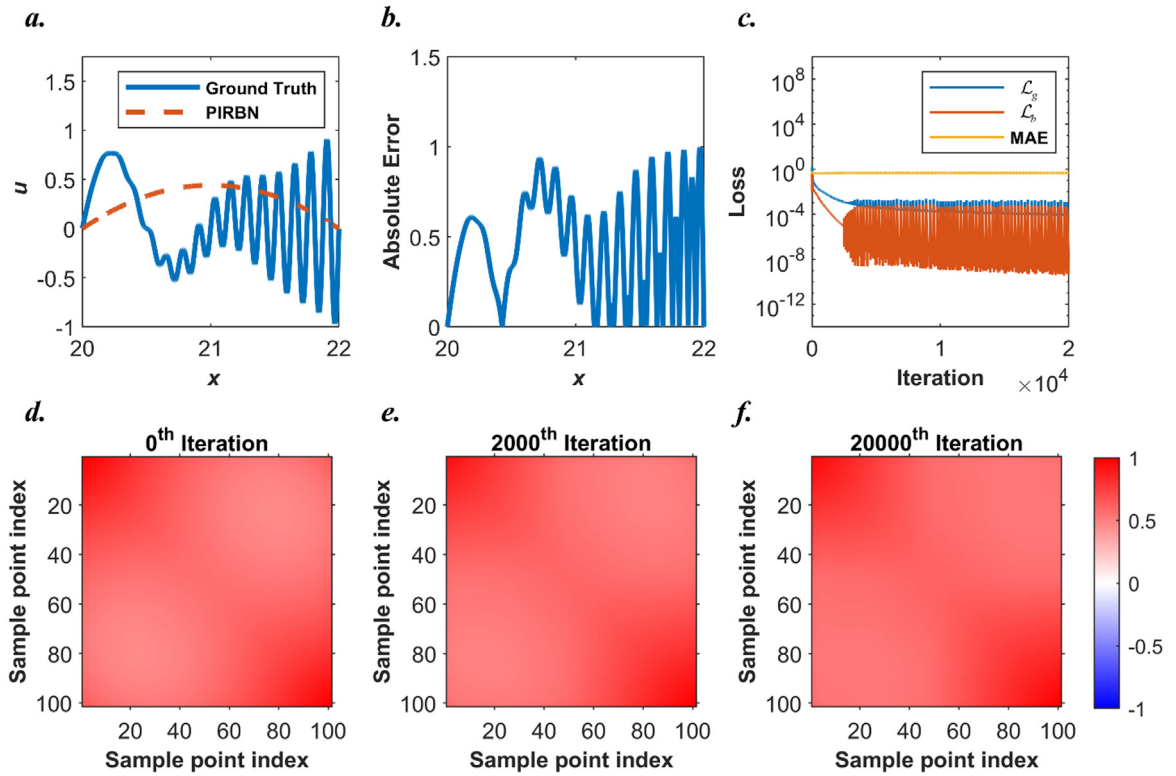


Fig. 18. Results from a PIRBN (single hidden layer with 101 neurons per layer) with the thin plate spline for solving Eq. (29). (a) Comparisons between the predictions from the PIRBN and the analytical solution. (b) Point-wise absolute error from the PIRBN. (c) Loss history of the PIRBN during the training process. (d) The normalised \mathbf{K}_g at the 0th iteration. (e) The normalised \mathbf{K}_g at the 2000th iteration; (f) The normalised \mathbf{K}_g at the 20000th iteration.

keep decreasing during the training process, while the loss terms from PINN remain nearly unchanged during the training process, as shown in Fig. 19(c) and (f). PINN requires 608 s while PIRBN requires 902 s for the entire training process, indicating that PIRBNs require more CPU time than PINNs with the same number of neurons for the same number of training iterations. Despite its excellent computational efficiency, PINN is unable to tackle this problem. Therefore, it is evident that the PIRBN is more effective for solving PDEs with high-frequency features and long-range domains compared to the original PINN.

4.2. Wave equation

Next, we extend the use of PIRBN to 2D problems. Consider the following 2D wave equation and the corresponding boundary conditions as

$$\begin{aligned} & \left(\frac{\partial^2}{\partial x^2} - 4 \frac{\partial^2}{\partial y^2} \right) u(x, y) = 0, \text{ for } x \in [0, 1], y \in [0, 1], \\ & u(x, 0) = u(x, 1) = \frac{\partial}{\partial x} u(0, y) = 0, \\ & u(0, y) = \sin(\pi y) + \frac{1}{2} \sin(4\pi y). \end{aligned} \tag{33}$$

The analytical solution is given as

$$u(x, y) = \cos(2\pi x) \sin(\pi y) + \frac{1}{2} \cos(8\pi x) \sin(4\pi y). \tag{34}$$

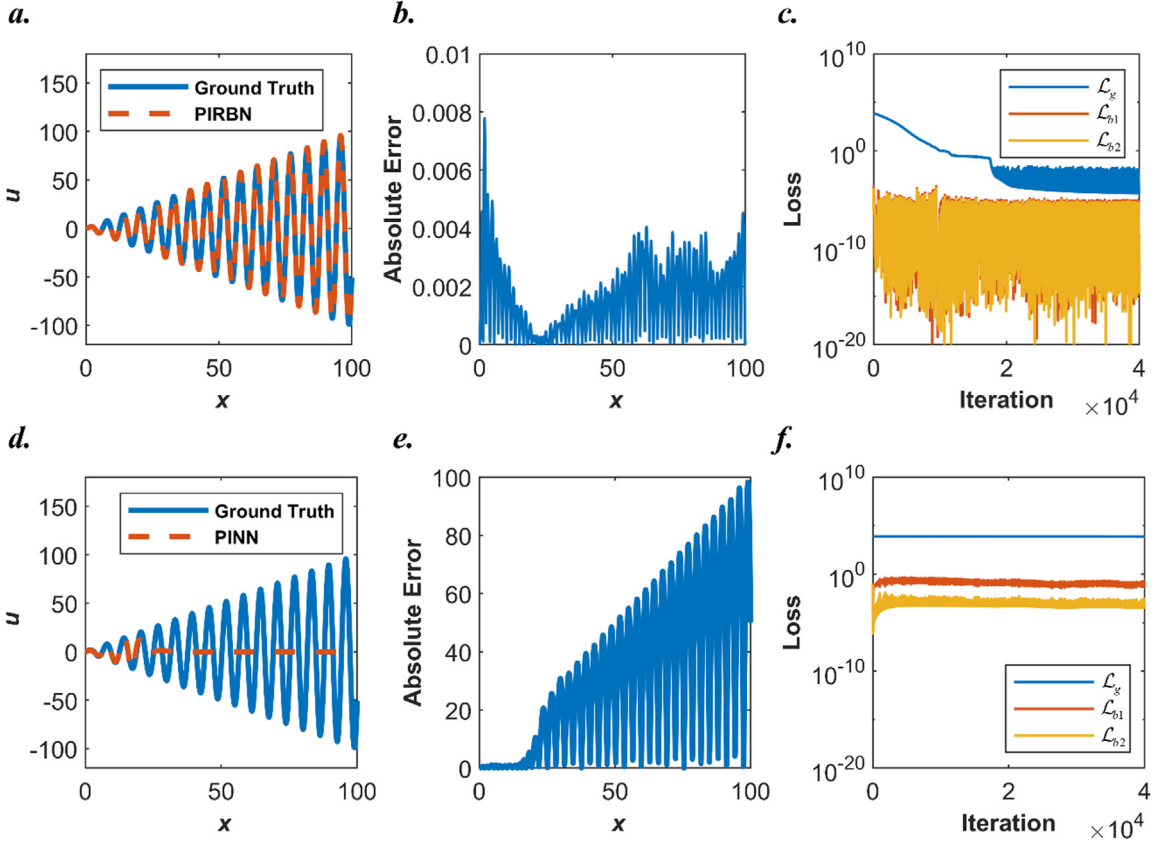


Fig. 19. Results for 1D nonlinear spring equation. (a) Comparison between the prediction from the PIRBN and the analytical solution. (b) Point-wise absolute error from the PIRBN. (c) Loss history of the PIRBN during the training process. (d) Comparison between the prediction from the PINN and the analytical solution. (e) Point-wise absolute error from the PINN. (f) Loss history of the PIRBN during the training process.

This problem is quite challenging due to the existence of high-frequency feature. Here, we apply a single-layer PIRBN with 61×61 neurons to solve this problem. The centres of neurons are uniformly distributed within computational domain $x \in [-0.1, 1.1]$, $y \in [-0.1, 1.1]$, where the spacing of neurons is 0.02. The initial b is set to 20. Besides, a PINN with the same number of hidden layer and neurons is also applied for comparison.

Fig. 20 shows the results from PIRBN for the wave equation. As observed, the predictions from PIRBN agree well with the analytical solution, while the maximum point-wise absolute error is 6×10^{-4} . The training process converges after approximately 8×10^3 iterations, as shown in Fig. 20(d). Besides, a PINN with a same size neural network is applied to solve this problem for comparison, and its results are shown in Fig. 21. It is clear to find that the PINN fails to predict the solution of the wave equation and its loss terms hardly change during the training process. It is also worth highlighting that, to address this problem via PINN, Wang et al. [51] applied an FNN with 5 hidden layers and 500 neurons per layer. Although a larger size FNN can produce good quality prediction, the maximum point-wise absolute error is still roughly 5×10^{-3} [51], which is significantly larger than it was obtained by the PIRBN.

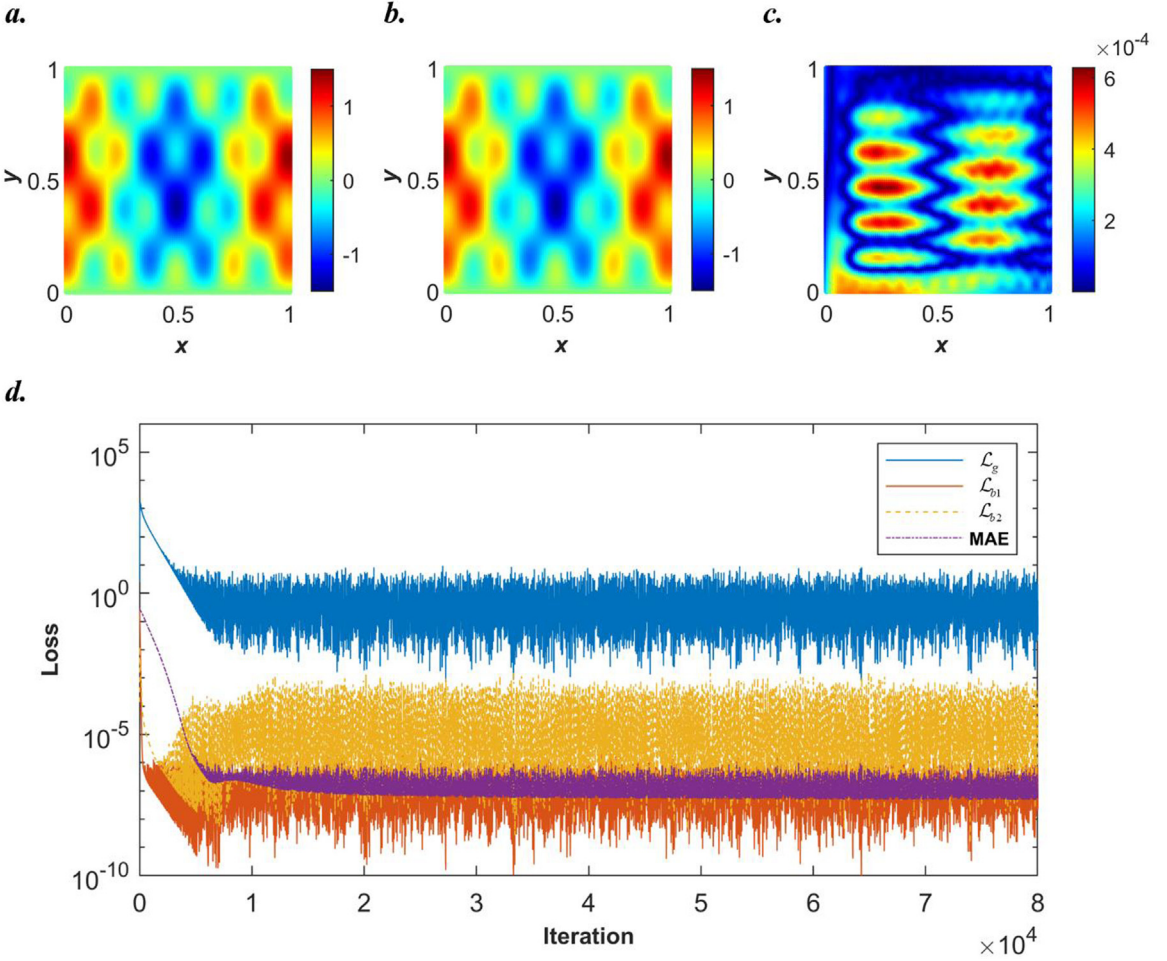


Fig. 20. PIRBN results for the 2D wave equation. (a) The prediction from the PIRBN. (b) The analytical solution. (c) Point-wise absolute error from the PIRBN. (d) Loss history and mean absolute error (MAE) of the PIRBN during the training process.

4.3. Diffusion equation

The diffusion equation is prevailingly seen in engineering, e.g., hydrodynamics [64] and heat transfer problems [65]. Consider a diffusion equation with its initial/boundary conditions as

$$\begin{aligned} \left(\frac{\partial}{\partial t} - 0.01 \frac{\partial^2}{\partial x^2} \right) u(x, t) &= g(x, t), \text{ for } x \in [5, 10], t \in [5, 10] \\ u(5, t) &= b_1(t), \\ u(10, t) &= b_2(t), \\ u(x, 5) &= b_3(x), \end{aligned} \quad (35)$$

where $g(x, t)$, $b_1(t)$, $b_2(t)$, and $b_3(x)$ are tailored functions. The solution $u(x, t)$ can be written as

$$u(x, t) = \left[2 \cos \left(\pi x + \frac{\pi}{5} \right) + \frac{3}{2} \cos \left(2\pi x - \frac{3\pi}{5} \right) \right] \left[2 \cos \left(\pi t + \frac{\pi}{5} \right) + \frac{3}{2} \cos \left(2\pi t - \frac{3\pi}{5} \right) \right]. \quad (36)$$

This problem is challenging for PINN due to the existence of the high-frequency feature and ill-posed computational domain. It is solved in [43] by domain decomposition, i.e., the whole computational domain is partitioned into subsections and local neural networks are used to respectively approximate the solutions within the corresponding subsections. Here, we apply a single-layer PIRBN with 61×61 RBF neurons to solve this problem. The centres

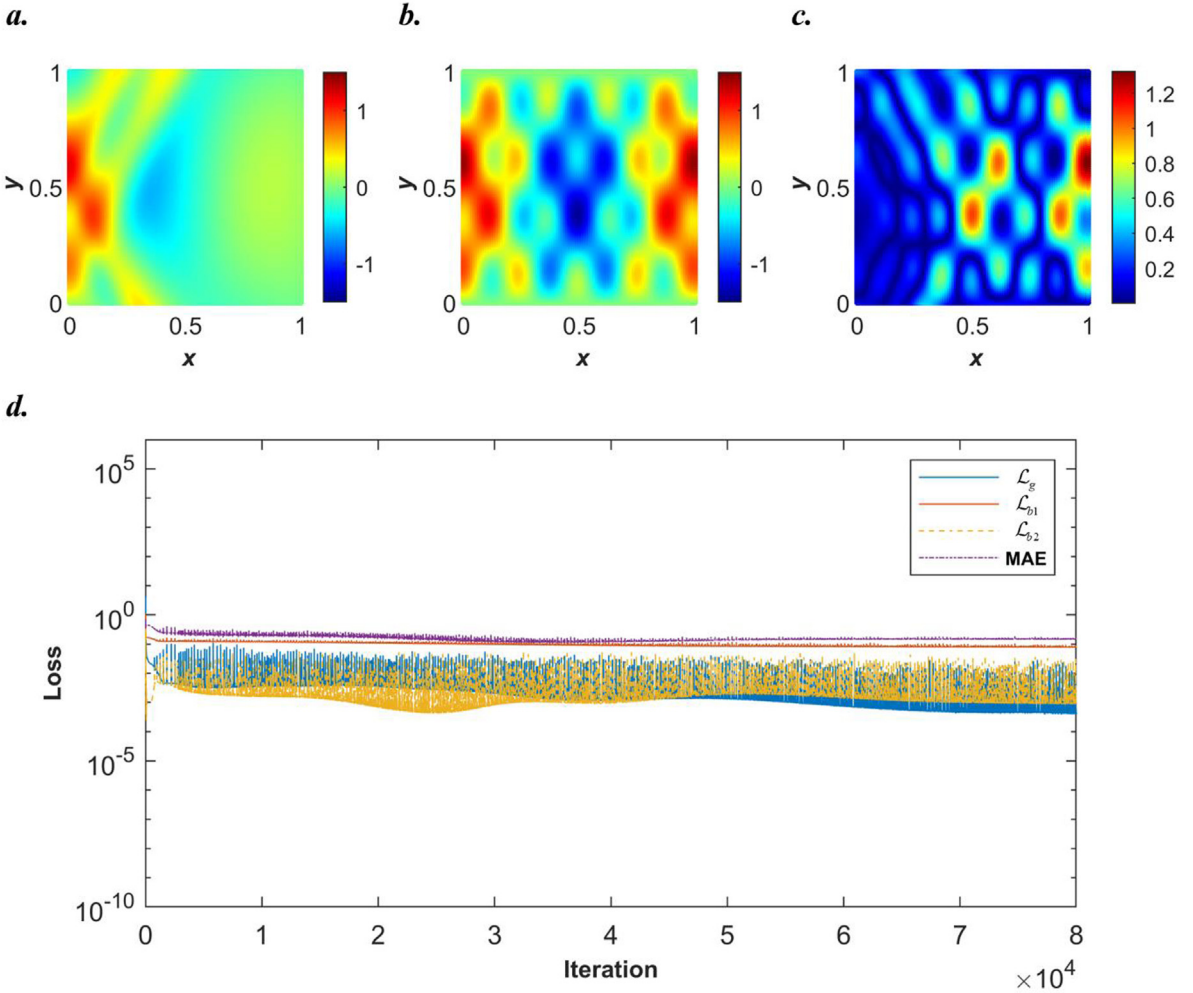


Fig. 21. PINN results for the 2D wave equation. (a) The prediction from the PINN. (b) The analytical solution. (c) Point-wise absolute error from the PINN. (d) Loss history and mean absolute error (MAE) of the PINN during the training process.

of the RBF neurons are uniformly distributed within domain $x \in [4.5, 10.5]$, $t \in [4.5, 10.5]$, where the spacing of neurons is 0.05. The initial b is set to 5. Besides, a PINN with the same number of hidden layer and neurons is also applied for comparison.

Fig. 22 shows the results from the PIRBN for solving the diffusion equation and Fig. 23 present the results from a PINN with a same size neural network for comparisons. As observed from Fig. 22(a)–(c), the PIRBN learns the solution well, while the maximum point-wise absolute error is 8×10^{-3} . On contrary, the PINN fails to learn the solution. Furthermore, as shown in Fig. 22(d) and Fig. 23(d), the training process of the PIRBN nearly converges after 2×10^4 iterations, while the loss terms of the PINN barely change during the whole training process.

4.4. Viscoelastic Poiseuille problem

Finally, a viscoelastic Poiseuille flow problem is used to test the performance of PIRBN. Viscoelastic flow is widely observed in nature and is hard to model due to its complexity [66]. Herein, an upper-convected Maxwell (UCM) fluid is used in this problem. The governing equations and the corresponding initial/boundary conditions

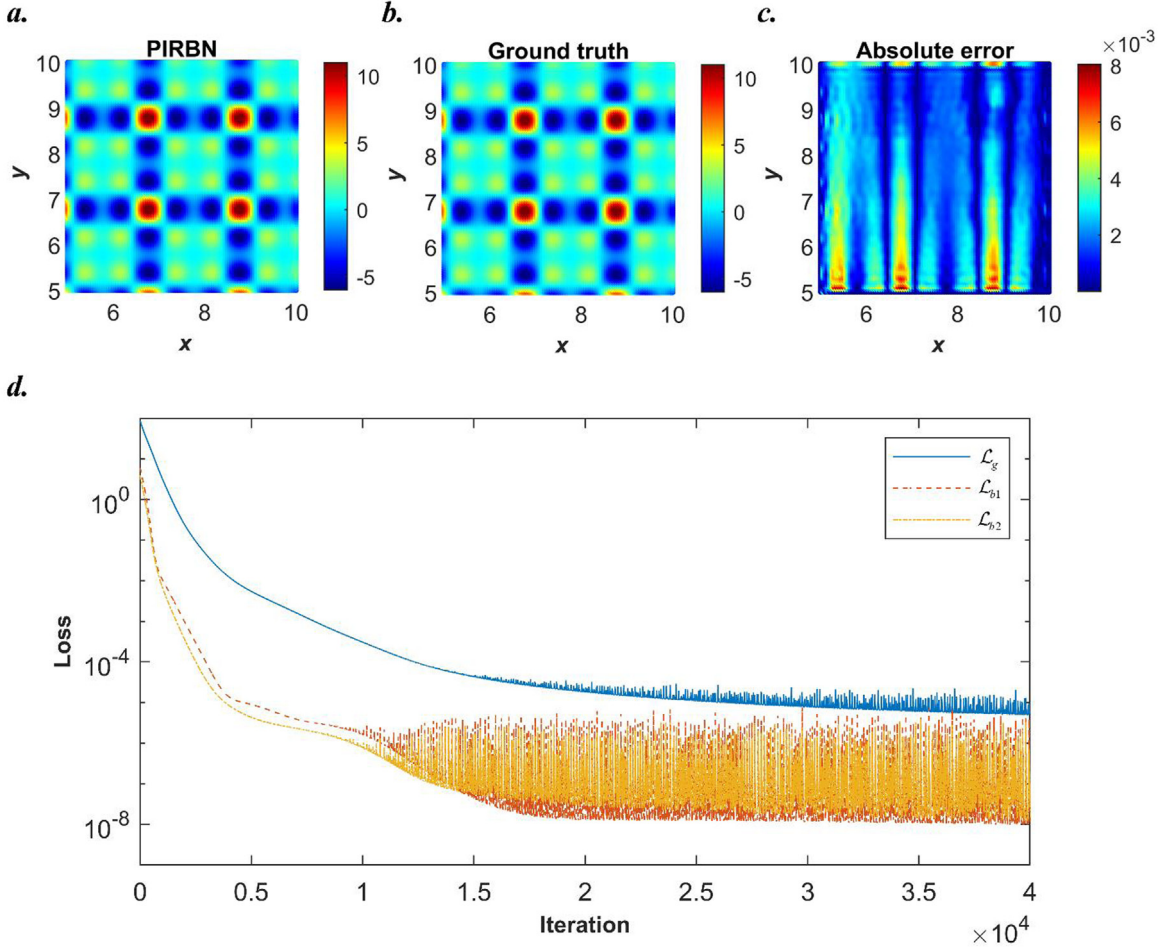


Fig. 22. PIRBN results for the diffusion equation. (a) The prediction from the PIRBN. (b) The analytical solution. (c) Point-wise absolute error from the PIRBN. (d) Loss history of the PIRBN during the training process.

are given as

$$\begin{cases} \rho \frac{\partial}{\partial t} u(y, t) = -f + \frac{\partial}{\partial y} \tau_{xy}(y, t), \\ \eta_0 \frac{\partial}{\partial y} u(y, t) = \left(\lambda \frac{\partial}{\partial t} + 1 \right) \tau_{xy}(y, t), \end{cases} \quad \text{for } t \in [0, 4], y \in [-0.5, 0.5] \quad (37)$$

$$u(\pm 0.5, t) = u(y, 0) = 0,$$

$$\tau_{xy}(y, 0) = 0,$$

where $f = -1.5$ N/m is the constant pressure gradient, τ_{xy} is the shear stress, $\rho = 1/3$ is the density of the fluid, $\eta_0 = 0.5$ is the viscosity of the fluid, $\lambda = 1/3$ is the relaxation time. The analytical solution is given in Appendix C. In this problem, the evolution contours of physical fields in terms of velocity and shear stress exhibit sharp transition shapes, which are challenging to be captured by PINN. To address the problem, we apply two PIRBNs and each PIRBN contains 26×101 RBF neurons that are uniformly distributed within the domain $t \in [-0.2, 4.2]$, $y \in [-0.7, 0.7]$. The spacing of RBF neurons is 0.04. The initial b is set to 20. Besides, a PINN with the same number of hidden layer and neurons is also applied for comparison.

Fig. 24 shows the results from the two PIRBNs trained by the Adam optimiser after 10^4 iterations (learning rate 0.001). For comparison, the predictions by using PINNs are provided in Fig. 25. As shown in Fig. 24(a)–(d), the evolutions of physics fields in terms of velocity and shear stress are well predicted by the two PIRBNs. The

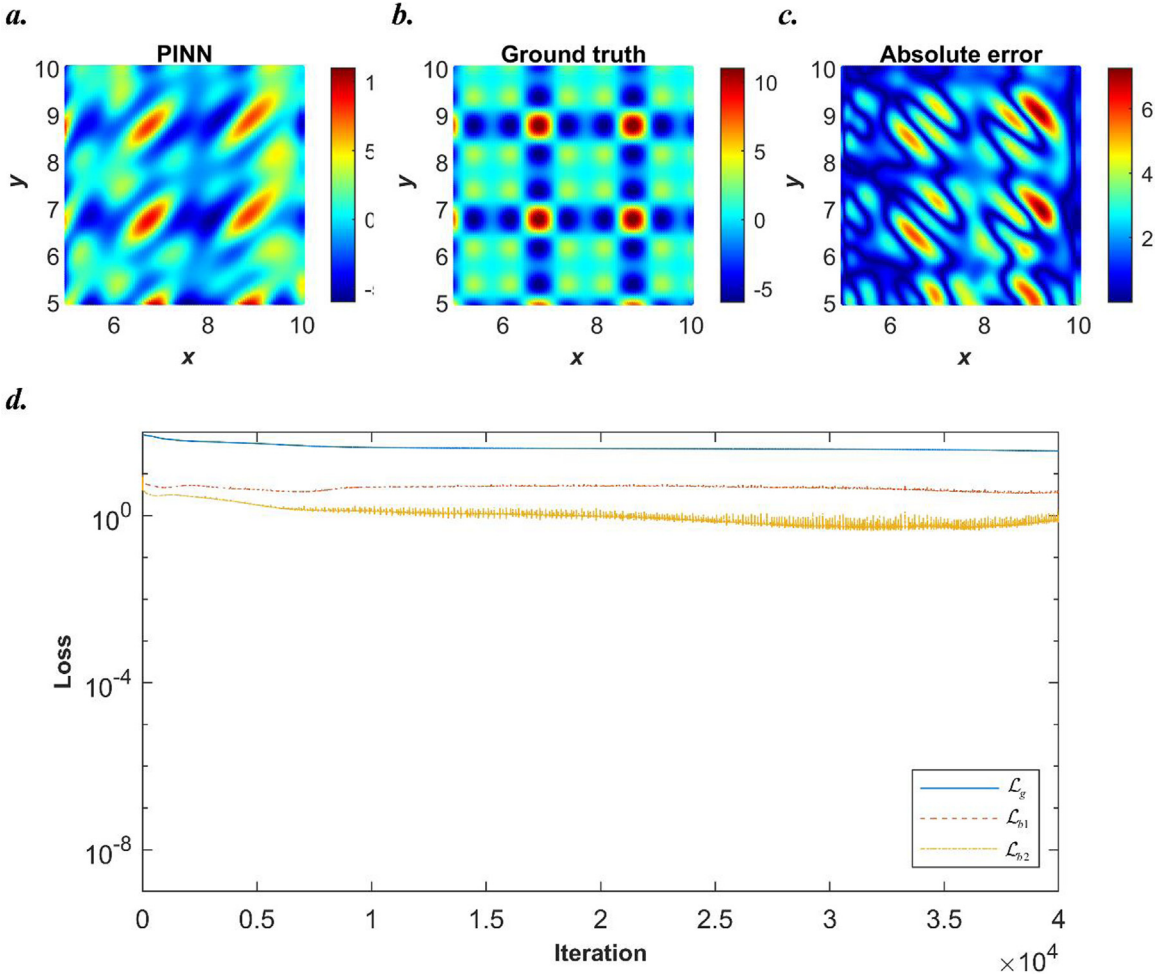


Fig. 23. PINN results for the diffusion equation. (a) The prediction from the PINN. (b) The analytical solution. (c) Point-wise absolute error from the PINN. (d) Loss history of the PINN during the training process.

high accuracies of PIRBNs are further demonstrated by the point-wise absolute error contours, which are shown in Fig. 24(e) and (f). On the other hand, predictions from the PINNs fail to capture the sharp transition shapes for velocity and shear stress fields, as shown in Fig. 25(a)–(d). Furthermore, the point-wise absolute error contours from the PINNs show the large deviations between the PINNs' prediction and the analytical solutions. Finally, by comparing the training histograms shown in Figs. 24(g) and 25(g), the PIRBNs achieve lower final losses than the PINNs. The training of the PIRBNs approximately converges after 5000 iterations.

5. Conclusion

In this work, based on the observation that PINNs tend to be local approximators after training, we proposed the physics-informed radial basis network (PIRBN) that can effectively solve PDEs suffering from high-frequency features and ill-posed computational domains. Meanwhile, we proved that training a PIRBN can converge to Gaussian process with a wide-enough neural network and studied the training dynamics of PIRBN using the NTK theory. The proposed PIRBN regarding the initialisation strategies, sizes of sample points and selections of RBF neurons are investigated in details. In the numerical examples, four challenging PDEs with high-frequency features and ill-posed computational domains are used to test the performances of the proposed PIRBN with respect to the original PINN. Compared to PINN, the proposed PIRBN is more effective than PINN for solving PDEs, which

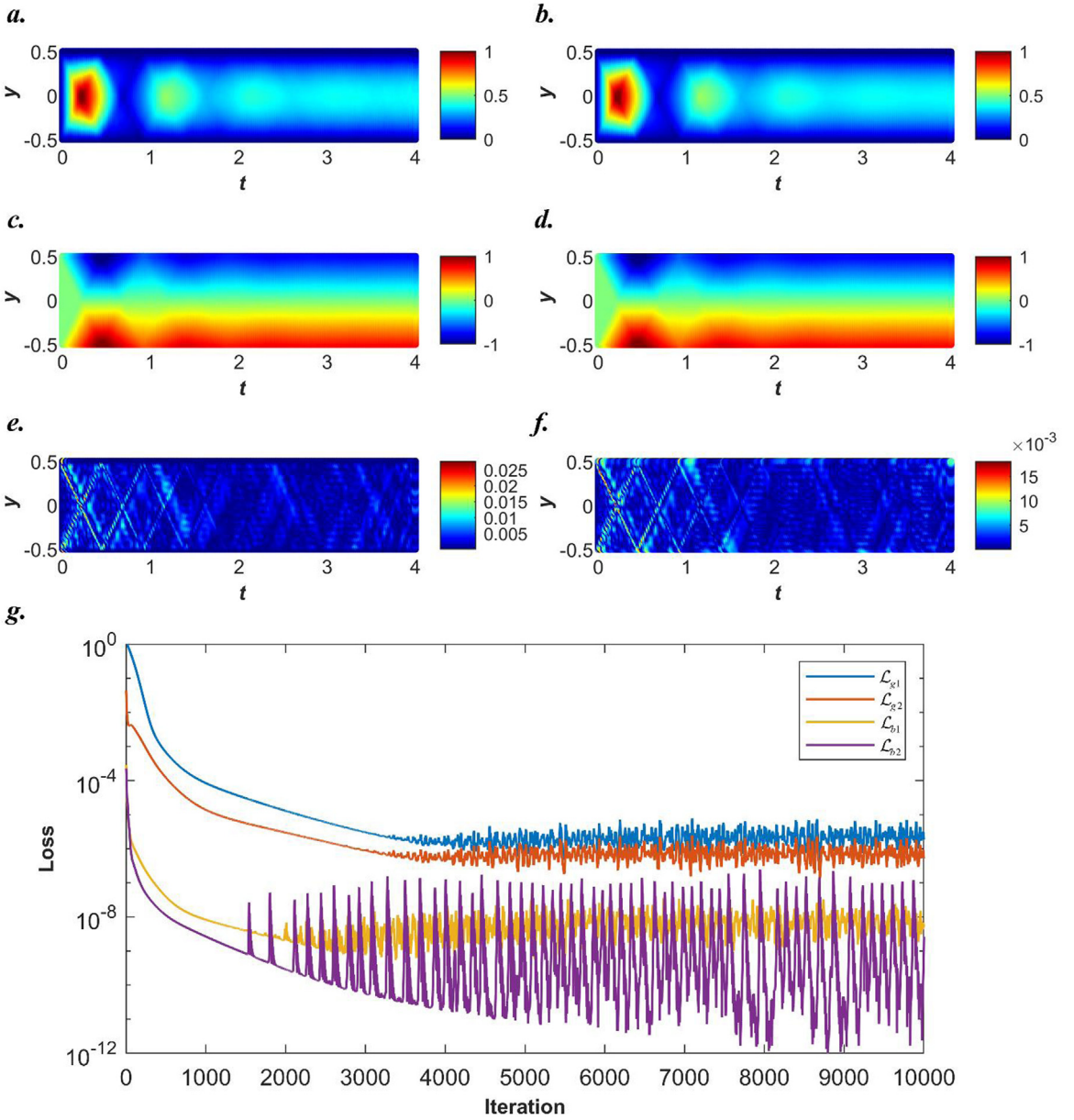


Fig. 24. Results from two PIRBNs for the UCM Poiseuille flow problem. (a) The velocity u predicted by the PIRBN. (b) The analytical solution of the velocity u . (c) The shear stress τ_{xy} predicted by the PIRBN. (d) The analytical solution of the shear stress τ_{xy} . (e) The point-wise absolute error of the velocity u predicted by the PIRBN. (f) The point-wise absolute error of the shear stress τ_{xy} predicted by the PIRBN. (g) Loss history of the PIRBN during the training process.

exhibit high-frequency features or suffer from ill-posed computational domains. Furthermore, most advanced PINN techniques, for example, adaptive sampling strategies [62,63] and transfer learning [67], can be directly integrated into the proposed PIRBN.

We notice that the proposed PIRBN shares some commonalities with collocation methods based on RBFs [68–70], such as the RBF collocation, the radial point interpolation method (RPIM) and the radial point interpolation collocation method (RPICM). Despite the use of RBFs, the PIRBN and the RBFs-based collocation methods are

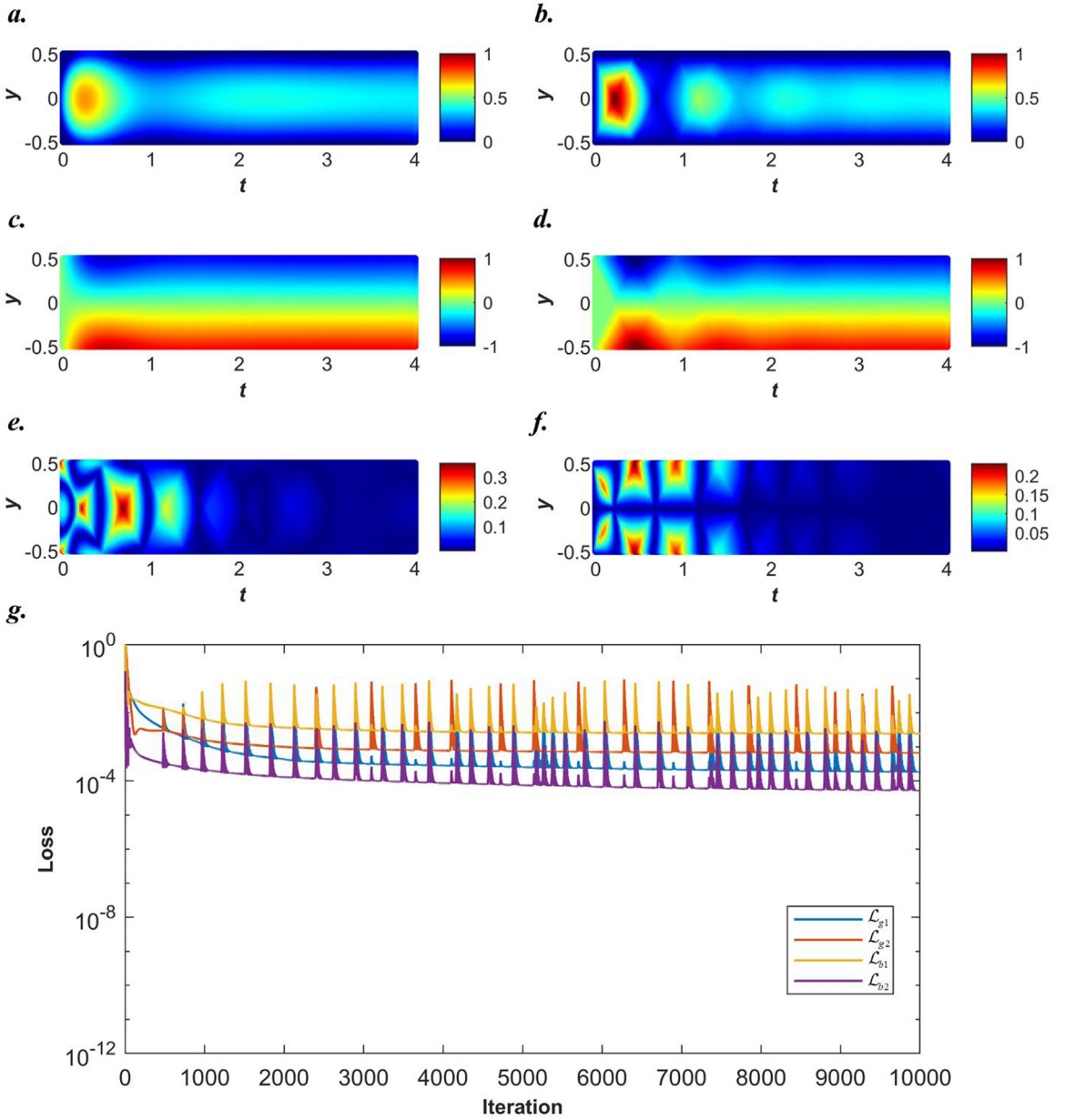


Fig. 25. Results from two PINNs for the UCM Poiseuille flow problem. (a) The velocity u predicted by the PINN. (b) The analytical solution of the velocity u . (c) The shear stress τ_{xy} predicted by the PINN. (d) The analytical solution of the shear stress τ_{xy} . (e) The point-wise absolute error of the velocity u predicted by the PINN. (f) The point-wise absolute error of the shear stress τ_{xy} predicted by the PINN. (g) Loss history of the PINN during the training process.

intrinsically different. First of all, the implementation procedures of them for solving PDEs are different. The RBFs-based collocation methods directly implement PDEs via collocation methods, and hence can suffer from issues regarding stability (if the collocations use local nodes) and scalability (if all the nodes in the domain are used) [71]. In fact, great efforts are still being made to overcome these issues. The proposed PIRBN controls the solution of PDEs by a functional (L2 norm type loss function), which removes negativity and improves the stability of the

solving process [72]. Then, the accuracy of an RBF collocation method heavily depends on the shape parameters used in RBF [71,73]. The shape parameters need to be carefully tuned for the desired accuracy. More importantly, such a shape-parameter-tuning is problem-dependent and hence is quite a challenging task. In the proposed PIRBN, these shape parameters can be automatically modified during training. Finally, the proposed PIRBN made good use of the features of RBFs and neural networks. Therefore, the proposed PIRBN is more powerful and can perform better than the RBFs-based collocation methods in solving PDEs, especially for strong nonlinear problems and highly coupled multi-physics fields.

Yet, it is also important to note that the current PIRBN is limited to fixed centres for all neurons and a single hidden layer structure, whereas the advantageous performance of DL is enhanced by several hidden layers. Merely adding more hidden layers to the PIRBN without further modifications may conflict with the valuable local approximation property. To take advantage of the power of multiple hidden layers, studies on how to properly integrate multiple hidden layers to the current PIRBN are encouraged. Besides, more investigation regarding using “deep” structures, which can make neural networks exhibit the local approximation property, is suggested. Apart from the neural network, it is also of significance to explore the initialisation schemes that can enhance the local approximation property of neural networks. Moreover, since the PIRBN enjoys great local properties along with the training process, specific training strategies can be proposed to boost the training efficiency. These topics will be addressed in our future work.

CRediT authorship contribution statement

Jinshuai Bai: Conceptualization, Methodology, Coding, Formal analysis, Writing – original draft. **Gui-Rong Liu:** Advising, Scientific discussions, Writing – review & editing. **Ashish Gupta:** Writing – review & editing. **Laith Alzubaidi:** Writing – review & editing. **Xi-Qiao Feng:** Writing – review & editing. **YuanTong Gu:** Conceptualization, Writing – review & editing, Supervision.

Declaration of competing interest

The authors declare that they have no known competing financial interests or personal relationships that could have appeared to influence the work reported in this paper.

Data availability

We have uploaded our data and code on Github. Anyone can freely access to them.

Acknowledgements

Support from the Australian Research Council research grants (IC190100020 and DP 200102546) is gratefully acknowledged (J. Bai and Y.T. Gu).

Appendix A. NTK change of PINN with multilayer FNN

PINNs with multiple hidden layers FNN also exhibit the local approximation property during the training process. Herein, consider the PDE problem stated as Eq. (13) when $\mu = 4$, an FNN is constructed with three hidden layers and 61 neurons per layer. 101 sample points are uniformly distributed inside the computational domain. The neural network is trained by the Adam optimiser with a learning rate of 0.001.

Fig. A.1 shows the results from the multilayer FNN after 2×10^4 iterations. The prediction from the FNN aligns well with the analytical solution, while the largest point-wise error is less than 0.02. Besides, as observed from Fig. A.1(d)–(f), the diagonal elements of the PINN’s NTK exhibit the similar local approximating behaviour as observed when using “shallow” neural networks, despite slight oscillations (shadow blue and red colours) in the rest area. The slight oscillations in the rest area are worth further investigating, however it is out of the scope of this work.

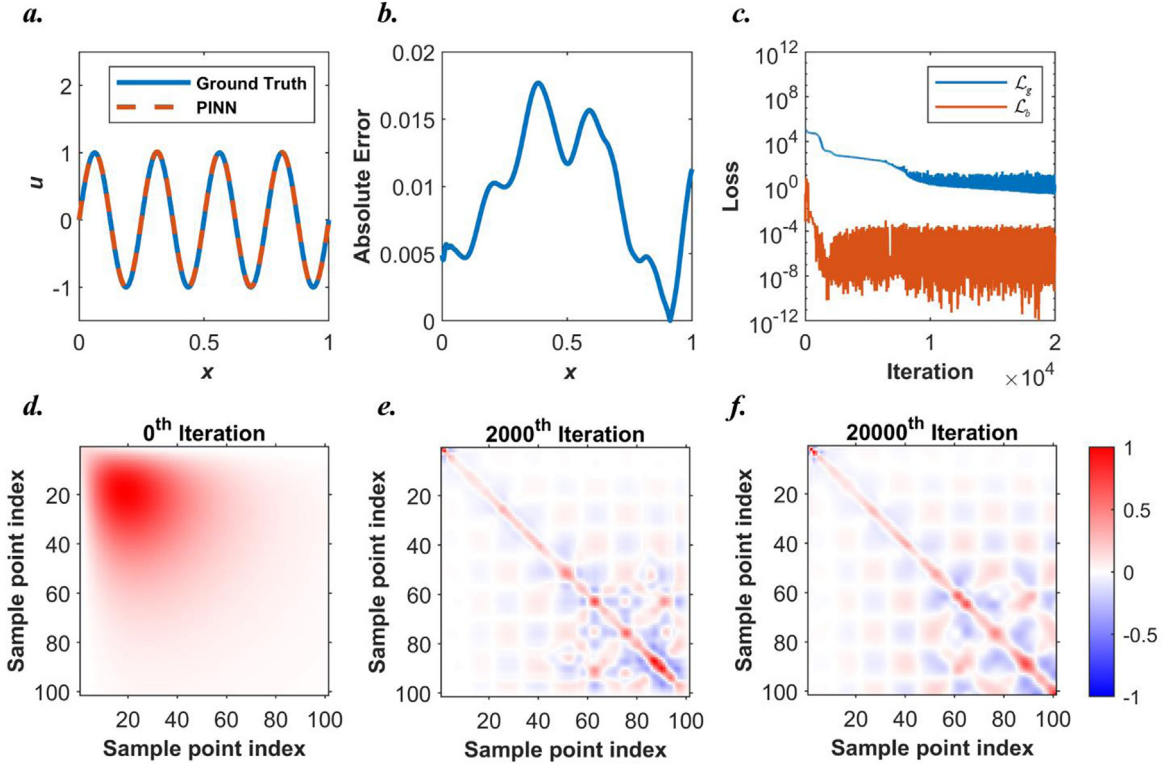


Fig. A.1. Results from a PINN (three hidden layers with 61 neurons per layer) for solving Eq. (13) when $\mu = 4$. (a) Comparisons between the PINN predictions and the ground truth. (b) Point-wise absolute error plot. (c) Loss history of the PINN during the training process. (d) The normalised \mathbf{K}_g at 0th iteration. (e) The normalised \mathbf{K}_g at 2000th iteration. (f) The normalised \mathbf{K}_g at 20000th iteration. (For interpretation of the references to colour in this figure legend, the reader is referred to the web version of this article.)

To further demonstrate the local approximation property of PINN with multiple hidden layers FNNs during the training process, a 2D wave equation is applied

$$\begin{aligned} \left(\frac{\partial^2}{\partial x^2} - \frac{\partial^2}{\partial y^2} \right) u(x, y) &= 0, \text{ for } x \in [0, 1], y \in [0, 1], \\ u(x, 0) = u(x, 1) &= u(0, y) = 0, \\ \frac{\partial}{\partial x} u(0, y) &= 0. \end{aligned} \tag{A.1}$$

The analytical solution is given as

$$u(x, y) = \sqrt{2} \sin\left(4\pi x + \frac{\pi}{4}\right) \sin(4\pi y). \tag{A.2}$$

A PINN with three hidden layers and 30 neurons per layer is used to solve the problem. The Adam optimiser is applied to train the PINN for 8×10^4 iterations with a learning rate of 10^{-3} . Figs. A.2 and A.3 present the predictions from the PINN before and after training, respectively. Without training, as observed in Fig. A.2(a)–(c), the PINN obviously fail to predict the solution of the wave equation. As shown in Fig. A.2(d), the PINN at the initial stage exhibits poor local approximating property, where the \mathbf{K}_g contours for the 9 selected sample points (black crosses) are close to the value of 1, suggesting that the rest of all sample points are highly coupled with the selected sample points. After training, as shown in Fig. A.3(a)–(c), the PINN can predict the solution of the wave function at a maximum absolute point-wise error of roughly 0.09. Despite the complex patterns presented in Fig. A.3(d), dark red areas can be always observed around the selected sample points, suggesting that the surrounding sample points are better coupled with the selected sample points than the far-away sample points. This further demonstrates that PINNs tend to be local approximators during training processes.

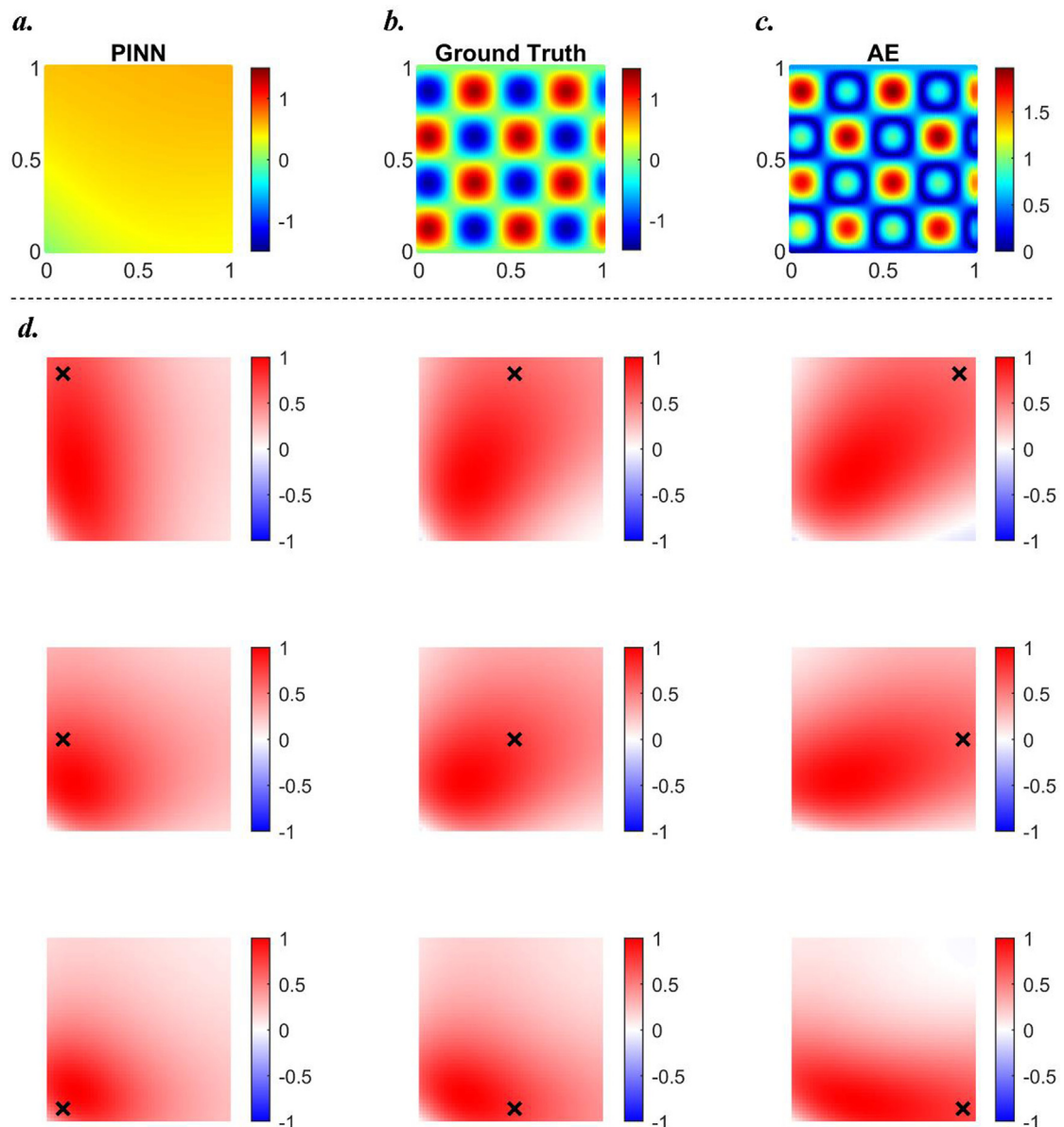


Fig. A.2. Predictions from a PINN (three hidden layers with 30 neurons per layer) for solving the 2D wave equation before training. (a) The prediction from the PINN. (b) The analytical solution. (c) Point-wise absolute error from the PINN. (d) The PINN's normalised K_g contours of 9 different sample points before training. Black crosses represent the position of the sample points.

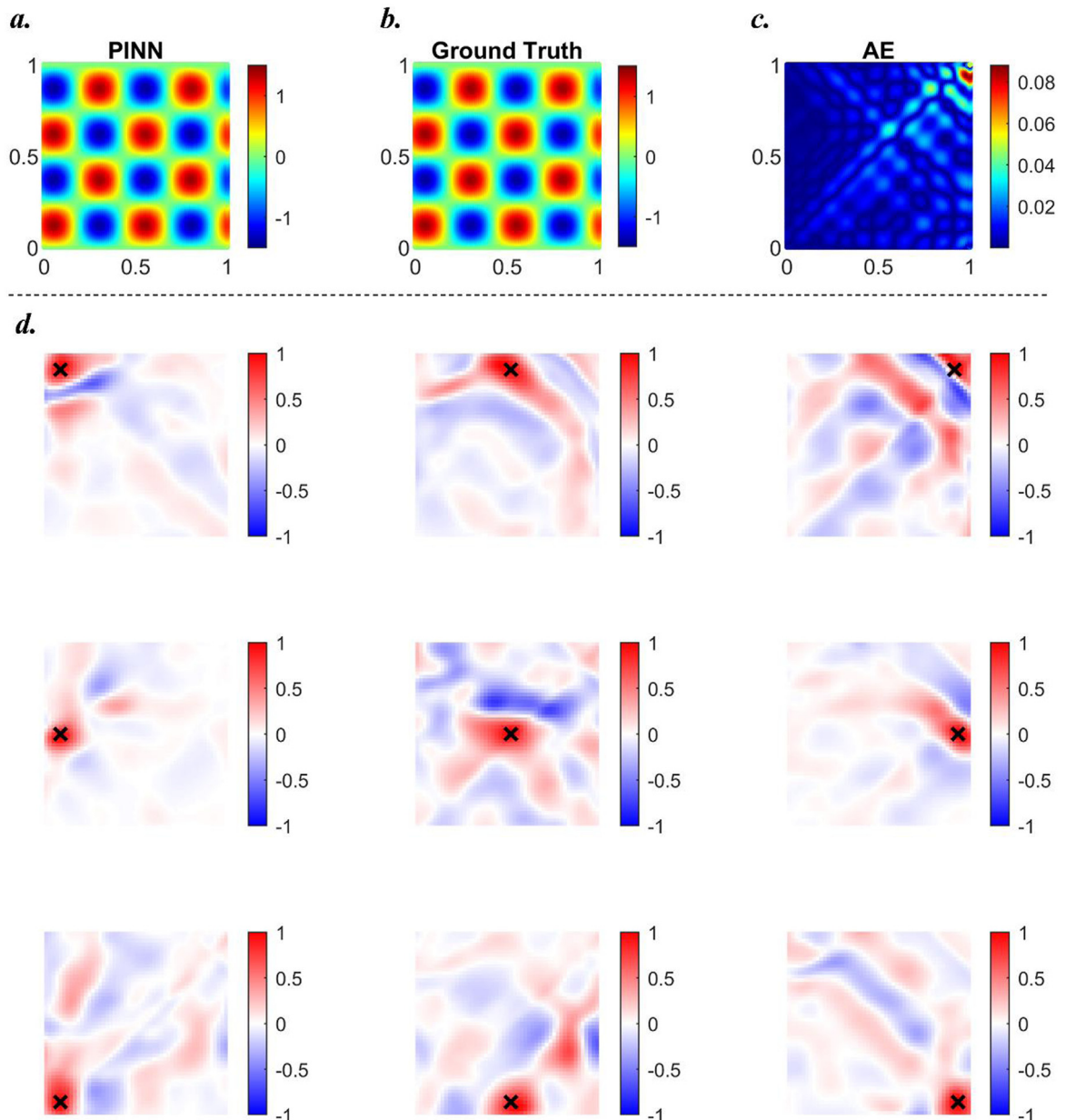


Fig. A.3. Predictions from a PINN (three hidden layers with 30 neurons per layer) for solving the 2D wave equation after training. (a) The prediction from the PINN. (b) The analytical solution. (c) Point-wise absolute error from the PINN. (d) The PINN's normalised K_g contours of 9 different sample points after training. Black crosses represent the sample points. (For interpretation of the references to colour in this figure legend, the reader is referred to the web version of this article.)

Appendix B. Proofs of theorems

B.1. Proof of Theorem 3.1.1

Proof. To solve the PDE stated as Eq. (15) by using a PIRBN with the Gaussian function, the second-order partial differential term, $\partial^2 u / \partial x^2$, can be mathematically written as

$$\begin{aligned} \frac{\partial^2}{\partial x^2} u(x, \theta) &= \frac{1}{\sqrt{d}} \sum_i^d a_i \ddot{\vartheta}_i(x, \theta) \\ &= \frac{1}{\sqrt{d}} \sum_i^d [-2a_i b_i^2 + 4a_i b_i^4 (x - c_i)^2] e^{-b_i^2 (x - c_i)^2} \end{aligned} \quad (\text{B.1})$$

Recall that all a_i are initialised as i.i.d. random variables satisfy $\mathcal{N}(0, 1)$ distribution, b_i and c_i are initialised by given constants. Then, by the central limit theorem, we obtain

$$\mathbb{E}[a \ddot{\vartheta}(x)] \sim \mathcal{N}(0, \Sigma(x)), \quad (\text{B.2})$$

where

$$\Sigma(x) = \text{Var}[a_i \ddot{\vartheta}(x)]. \quad (\text{B.3})$$

This can be further proved by numerical examples, as shown in Fig. B.1. Note that $e^{-b_i^2 (x - c_i)^2} \in (0, 1]$,

$$\begin{aligned} \sup_d \mathbb{E} \left[\left| \frac{\partial^2}{\partial x^2} u(x, a, b) \right|^2 \right] &= \mathbb{E} \left[\frac{1}{d} \sum_i^d a_i^2 (-2b_i^2 + 4b_i^4 (x - c_i)^2)^2 e^{-2b_i^2 (x - c_i)^2} \right] \\ &\leq \mathbb{E} \left[\frac{1}{d} \sum_i^d a_i^2 (-2b_i^2 + 4b_i^4 (x - c_i)^2)^2 \right] \\ &= \mathbb{E} \left[a_i^2 (-2b_i^2 + 4b_i^4 (x - c_i)^2)^2 \right] < \infty. \end{aligned} \quad (\text{B.4})$$

Thus, we can obtain

$$\begin{aligned} \Sigma_g(x, x') &\triangleq \text{Cov}\left(\frac{\partial^2 u(x)}{\partial x^2}, \frac{\partial^2 u(x')}{\partial x^2}\right) \\ &= \mathbb{E} \left[\left(\frac{\partial^2 u(x)}{\partial x^2} - \mathbb{E} \left[\frac{\partial^2 u(x)}{\partial x^2} \right] \right) \left(\frac{\partial^2 u(x')}{\partial x^2} - \mathbb{E} \left[\frac{\partial^2 u(x')}{\partial x^2} \right] \right) \right] \\ &= \mathbb{E} \left[\frac{1}{d} \sum_i^d a_i^2 \ddot{\vartheta}(x) \ddot{\vartheta}(x') \right] \\ &= \mathbb{E}_{a \sim \mathcal{N}(0, 1)} [a^2 \ddot{\vartheta}(x) \ddot{\vartheta}(x')], \end{aligned} \quad (\text{B.5})$$

which completes the proof.

B.2. Proof of Theorem 3.1.3

Proof. As defined by Eq. (6), $\mathbf{K}(0)$ is consist of $\mathbf{K}_{gg}(0)$, $\mathbf{K}_{gb}(0)$ and $\mathbf{K}_{bb}(0)$. Here, we start from $\mathbf{K}_{bb}(0)$. Recalling Eq. (7), for any two given inputs x and x' , we can calculate the corresponding element $K_{bb}(0)$ as

$$K_{bb}(0) = \left\langle \frac{dB[u(x; \theta(t))]}{d\theta}, \frac{dB[u(x'; \theta(t))]}{d\theta} \right\rangle, \quad (\text{B.6})$$

where $\theta = (a_i, b_i)$, $i = 1, 2, \dots, d$. Given that a PIRBN can be mathematically expressed as

$$u(x; \theta) = \frac{1}{\sqrt{d}} \sum_i^d a_i e^{-b_i^2 (x - c_i)^2}. \quad (\text{B.7})$$

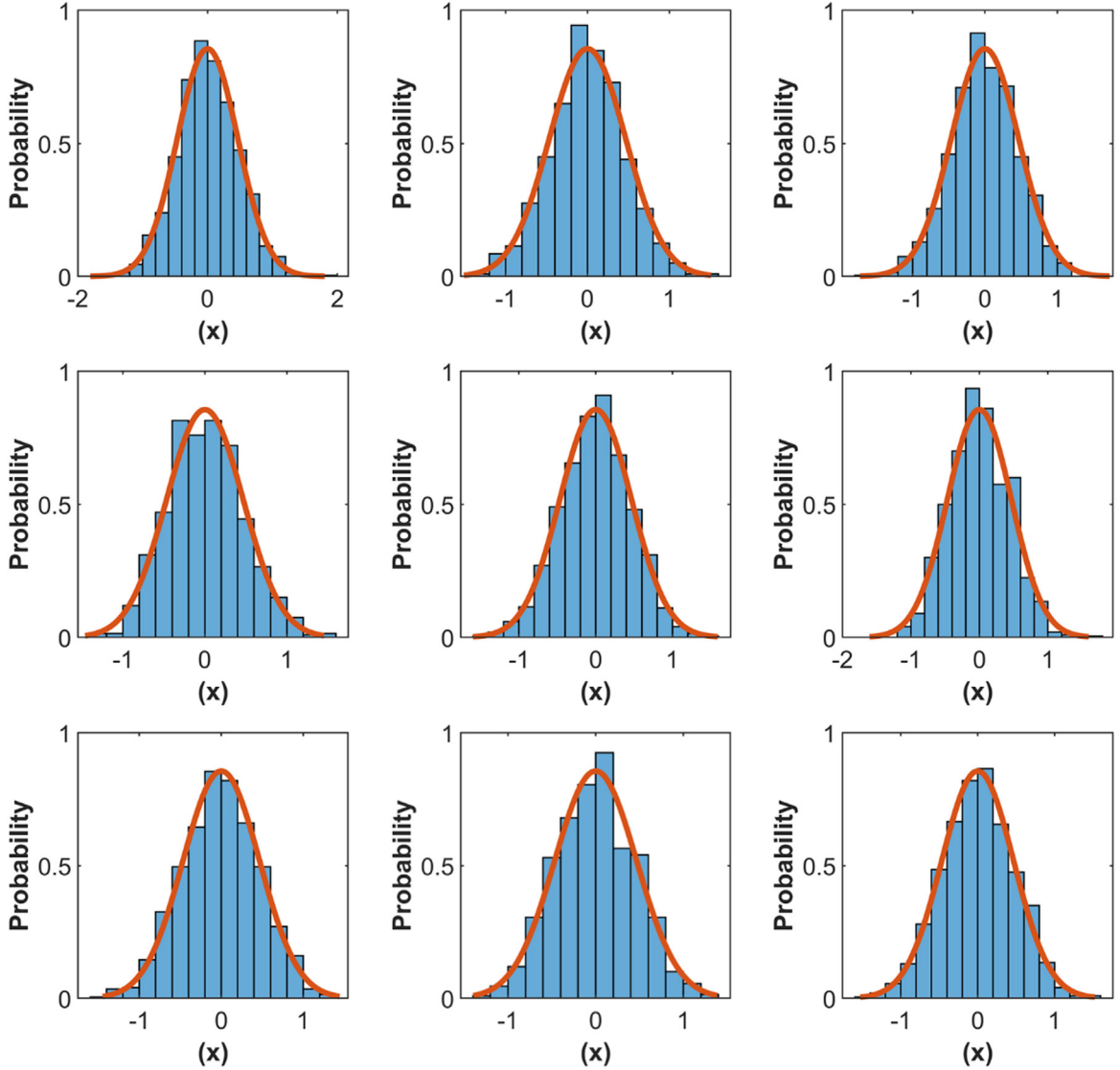


Fig. B.1. The distributions of 1000 values of $a_i \vartheta(x)$ from 9 times random initialisations, where blue columns represent the distribution values within a given range and red lines depict the reference Gaussian distribution. For each initialisation, the distribution of the 1000 values of $a_i \vartheta(x)$ exhibits the Gaussian distribution.

For simplicity, we pre-define

$$\Theta_i = e^{-b_i^2[(x-c_i)^2 + (x'-c_i)^2]} \in (0, 1]. \quad (\text{B.8})$$

Besides, a_i , b_i and c_i are independent variables to each other and $\mathbb{E}[a_i] = 1$. Therefore, by the central limit theorem, the $K_{\text{bb}}(0)$ can be further written as

$$K_{\text{bb}}(0) = \mathcal{A}_{\text{bb}} + \mathcal{B}_{\text{bb}}, \quad (\text{B.9})$$

where

$$\begin{aligned}
 \mathcal{A}_{\text{bb}} &= \sum_i^d \frac{\partial \mathbf{B}[u(x; \boldsymbol{\theta}(t))]}{\partial a_i} \frac{\partial \mathbf{B}[u(x'; \boldsymbol{\theta}(t))]}{\partial a_i} \\
 &= \frac{1}{d} \sum_i^d \Theta_i \\
 &= \mathbb{E}[\Theta], \\
 \mathcal{B}_{\text{bb}} &= \sum_i^d \frac{\partial \mathbf{B}[u(x; \boldsymbol{\theta}(t))]}{\partial b_i} \frac{\partial \mathbf{B}[u(x'; \boldsymbol{\theta}(t))]}{\partial b_i} \\
 &= -\frac{4}{d} \sum_i^d a_i^2 b_i^2 (x - c_i)^2 (x' - c_i)^2 \Theta_i \\
 &= -4\mathbb{E}[b^2 (x - c)^2 (x' - c)^2 \Theta],
 \end{aligned} \tag{B.10}$$

when $d \rightarrow \infty$. Thus, by substituting Eq. (B.10) into Eq. (B.9), we obtain

$$K_{\text{bb}}(0) = \mathbb{E}\left[\left(1 + 4b^2 (x - c)^2 (x' - c)^2\right) \Theta\right]. \tag{B.11}$$

Then, we target on $\mathbf{K}_{\text{gb}}(0)$. Again, for any two given inputs x and x' , we can calculate the corresponding element $K_{\text{gb}}(0)$ as

$$\begin{aligned}
 K_{\text{gb}}(0) &= \left\langle \frac{\partial \mathbf{G}[u(x; \boldsymbol{\theta}(t))]}{\partial \boldsymbol{\theta}}, \frac{\partial \mathbf{B}[u(x'; \boldsymbol{\theta}(t))]}{\partial \boldsymbol{\theta}} \right\rangle \\
 &= \mathcal{A}_{\text{gb}} + \mathcal{B}_{\text{gb}},
 \end{aligned} \tag{B.12}$$

where

$$\begin{aligned}
 \mathcal{A}_{\text{gb}} &= \sum_i^d \frac{\partial \mathbf{G}[u(x; \boldsymbol{\theta}(t))] \partial \mathbf{B}[u(x'; \boldsymbol{\theta}(t))]}{\partial a_i} \\
 &= \frac{2}{d} \sum_i^d (2b_i^2(x - c_i)^2 - b_i^2) \Theta_i \\
 &= 2\mathbb{E}\left[(2b^2(x - c)^2 - b^2)\Theta\right], \\
 \mathcal{B}_{\text{gb}} &= \sum_i^d \frac{\partial \mathbf{G}[u(x; \boldsymbol{\theta}(t))] \partial \mathbf{B}[u(x'; \boldsymbol{\theta}(t))]}{\partial b_i} \\
 &= \frac{8}{d} \sum_i^d a_i^2 b_i^2 (2b_i^4(x - c_i)^4 - 5b_i^2(x - c_i)^2 + 1) (x' - c_i)^2 \Theta_i \\
 &= 8\mathbb{E}\left[b^2 (2b^4(x - c)^4 - 5b^2(x - c)^2 + 1) (x' - c)^2 \Theta\right],
 \end{aligned} \tag{B.13}$$

when $d \rightarrow \infty$. Thus, by substituting Eq. (B.10) into Eq. (B.9), we obtain

$$K_{\text{gb}}(0) = \mathbb{E}\left[2\left((2b^2(x - c)^2 - b^2) + 4b^2(2b^4(x - c)^4 - 5b^2(x - c)^2 + 1)(x' - c)^2\right) \Theta\right]. \tag{B.14}$$

Finally, we focus on $\mathbf{K}_{\text{gg}}(0)$. For any two given inputs x and x' , we can calculate the corresponding element $K_{\text{gg}}(0)$ as

$$\begin{aligned}
 K_{\text{gg}}(0) &= \left\langle \frac{\partial \mathbf{G}[u(x; \boldsymbol{\theta}(t))]}{\partial \boldsymbol{\theta}}, \frac{\partial \mathbf{G}[u(x'; \boldsymbol{\theta}(t))]}{\partial \boldsymbol{\theta}} \right\rangle \\
 &= \mathcal{A}_{\text{gg}} + \mathcal{B}_{\text{gg}},
 \end{aligned} \tag{B.15}$$

where

$$\begin{aligned}
 \mathcal{A}_{gg} &= \sum_i^d \frac{\partial G[u(x; \theta(t))]}{\partial a_i} \frac{\partial G[u(x'; \theta(t))]}{\partial a_i} \\
 &= \frac{4}{d} \sum_i^d b_i^4 (2b_i^2(x - c_i)^2 - 1) (2b_i^2(x' - c_i)^2 - 1) \Theta_i \\
 &= 4\mathbb{E}[b^4 (2b^2(x - c)^2 - 1) (2b^2(x' - c)^2 - 1) \Theta], \\
 \mathcal{B}_{gg} &= \sum_i^d \frac{\partial G[u(x; \theta(t))]}{\partial b_i} \frac{\partial G[u(x'; \theta(t))]}{\partial b_i} \\
 &= \frac{16}{d} \sum_i^d a_i^2 b_i^2 (2b_i^4(x - c_i)^4 - 5b_i^2(x - c_i)^2 + 1) (2b_i^4(x' - c_i)^4 - 5b_i^2(x' - c_i)^2 + 1) \Theta_i \\
 &= 16\mathbb{E}[b^2 (2b^4(x - c)^4 - 5b^2(x - c)^2 + 1) (2b^4(x' - c)^4 - 5b^2(x' - c)^2 + 1) \Theta],
 \end{aligned} \tag{B.16}$$

when $d \rightarrow \infty$. Thus, by substituting Eq. (B.10) into Eq. (B.9), we obtain

$$\begin{aligned}
 K_{gg}(0) &= \mathbb{E}[4(b^4(2b^2(x - c)^2 - 1)(2b^2(x' - c)^2 - 1) + \\
 &\quad 4b^2(2b^4(x - c)^4 - 5b^2(x - c)^2 + 1)(2b^4(x' - c)^4 - 5b^2(x' - c)^2 + 1)) \Theta].
 \end{aligned} \tag{B.17}$$

Since b_i, c_i are initialised with given values, $K_{bb}(0)$, $K_{gb}(0)$ and $K_{gg}(0)$ are convergence to determinate values, which complete the proof.

B.3. Proof of Theorem 3.1.4

Proof. The NTK of the PIRBN can be written as

$$\mathbf{K}(t) = \mathbf{J}(t)\mathbf{J}^T(t), \tag{B.18}$$

where $\mathbf{J}(t)$ is the Jacobian matrix

$$\mathbf{J}(t) = \begin{bmatrix} \mathbf{J}_g(t) \\ \mathbf{J}_b(t) \end{bmatrix} = \begin{bmatrix} \frac{\partial G[u(x_i^g; \theta(t))]}{\partial \theta} \\ \frac{\partial B[u(x_i^b; \theta(t))]}{\partial \theta} \end{bmatrix}. \tag{B.19}$$

By substituting Eq. (B.19) into Eq. (23) and the Cauchy–Schwartz inequality, we have

$$\begin{aligned}
 \|\mathbf{K}(t) - \mathbf{K}(0)\|_2 &= \|\mathbf{J}(t)\mathbf{J}^T(t) - \mathbf{J}(0)\mathbf{J}^T(0)\|_2 \\
 &\leq \|\mathbf{J}(t)\|_2 \|\mathbf{J}(t) - \mathbf{J}(0)\|_2 + \|\mathbf{J}(t) - \mathbf{J}(0)\|_2 \|\mathbf{J}(0)\|_2
 \end{aligned} \tag{B.20}$$

Here, we start from $\|\mathbf{J}(t)\|_2$ first. Recalling Eq. (7), for any given inputs x , the two components of $\mathbf{J}(t)$ can be calculated as

$$\begin{aligned}
 \mathbf{J}_g(t) &= \begin{bmatrix} \frac{\partial G[u(x; \theta(t))]}{\partial a_i} & \frac{\partial G[u(x; \theta(t))]}{\partial b_i} \end{bmatrix} \\
 &= \begin{bmatrix} \frac{2}{\sqrt{d}} [2b_i^4(x - c_i)^2 - b_i^2] e^{-b_i^2(x - c_i)^2} \\ \frac{4a_i b_i}{\sqrt{d}} [5b_i^2(x - c_i)^2 - 2b_i^4(x - c_i)^4 - 1] e^{-b_i^2(x - c_i)^2} \end{bmatrix}^T, \\
 \mathbf{J}_b(t) &= \begin{bmatrix} \frac{\partial B[u(x; \theta(t))]}{\partial a_i} & \frac{\partial B[u(x; \theta(t))]}{\partial b_i} \end{bmatrix} \\
 &= \begin{bmatrix} \frac{1}{\sqrt{d}} e^{b_i^2(x - c_i)^2} & \frac{2a_i b_i}{\sqrt{d}} (x - c_i)^2 e^{b_i^2(x - c_i)^2} \end{bmatrix}
 \end{aligned} \tag{B.21}$$

Since $e^{-b_i^2(x - c_i)^2}$ and $a_i(t)$ are all bounded during the training process, $J_g(t)$ and $J_b(t)$ are bounded during the training process. Thus, $\|\mathbf{J}(t)\|_2$ also is bounded during the training process.

Then, we focus on $\|\mathbf{J}(t) - \mathbf{J}(0)\|_2$. For any given inputs x , the two components of $\|\mathbf{J}(t) - \mathbf{J}(0)\|_2$ can be written as

$$\begin{aligned}\|\mathbf{J}_b(t) - \mathbf{J}_b(0)\|_2 &= \left\| \frac{d\mathbf{B}[u(x; \boldsymbol{\theta}(t))]}{d\boldsymbol{\theta}} - \frac{d\mathbf{B}[u(x; \boldsymbol{\theta}(0))]}{d\boldsymbol{\theta}} \right\|_2, \\ \|\mathbf{J}_g(t) - \mathbf{J}_g(0)\|_2 &= \left\| \frac{d\mathbf{G}[u(x; \boldsymbol{\theta}(t))]}{d\boldsymbol{\theta}} - \frac{d\mathbf{G}[u(x; \boldsymbol{\theta}(0))]}{d\boldsymbol{\theta}} \right\|_2\end{aligned}\quad (\text{B.22})$$

For sake of simplicity, we pre-define following terms

$$\begin{aligned}\varepsilon_i &= (x - c_i)^2 \\ A_i(t) &= e^{-b_i^2(t)\varepsilon_i}, \\ B_i(t) &= a_i(t)b_i(t)\varepsilon_i A_i(t), \\ C_i(t) &= 2[2b_i^4(t)\varepsilon_i - b_i^2(t)]A_i(t), \\ D_i(t) &= 4a_i(t)b_i(t)[5b_i^2(t)\varepsilon_i - 2b_i^4(t)\varepsilon_i^2 - 1]A_i(t).\end{aligned}\quad (\text{B.23})$$

Thus, for $\|\mathbf{J}_b(t) - \mathbf{J}_b(0)\|_2$ we can obtain

$$\begin{aligned}&\left\| \frac{d\mathbf{B}[u(x; \boldsymbol{\theta}(t))]}{d\boldsymbol{\theta}(t)} - \frac{d\mathbf{B}[u(x; \boldsymbol{\theta}(0))]}{d\boldsymbol{\theta}(0)} \right\|_2 \\ &\leq \frac{2}{\sqrt{d}} \|\mathbf{A}(t) - \mathbf{A}(0)\|_2 + \frac{2}{\sqrt{d}} \|\mathbf{B}(t) - \mathbf{B}(0)\|_2, \\ &\left\| \frac{d\mathbf{G}[u(x; \boldsymbol{\theta}(t))]}{d\boldsymbol{\theta}(t)} - \frac{d\mathbf{G}[u(x; \boldsymbol{\theta}(0))]}{d\boldsymbol{\theta}(0)} \right\|_2 \\ &\leq \frac{1}{\sqrt{d}} \|\mathbf{C}(t) - \mathbf{C}(0)\|_2 + \frac{1}{\sqrt{d}} \|\mathbf{D}(t) - \mathbf{D}(0)\|_2.\end{aligned}\quad (\text{B.24})$$

We first focus on $\frac{2}{\sqrt{d}} \|\mathbf{A}(t) - \mathbf{A}(0)\|_2$. Note that the evolution of $\boldsymbol{\theta}(t)$ between t_i and t_{i+1} iterations using gradient descendent algorithms can be written as

$$\frac{\boldsymbol{\theta}(t_{i+1}) - \boldsymbol{\theta}(t_i)}{\eta} = -\nabla \mathcal{L}(\boldsymbol{\theta}), \quad (\text{B.25})$$

where η is the learning rate. With infinitesimally small learning rate, we can obtain the gradient flow as

$$\frac{d\boldsymbol{\theta}}{dt} = \frac{d\boldsymbol{\theta}}{d\mathbf{A}} \frac{d\mathbf{A}}{dt} = -\nabla \mathcal{L}(\boldsymbol{\theta}). \quad (\text{B.26})$$

By Eq. (B.26), we can obtain

$$\begin{aligned}&\frac{2}{\sqrt{d}} \|\mathbf{A}(t) - \mathbf{A}(0)\|_2, \\ &= \frac{2}{\sqrt{d}} \left\| \int_0^t \frac{d\mathbf{A}(\sigma)}{d\sigma} d\sigma \right\|_2 \\ &= \frac{2}{\sqrt{d}} \left\| \int_0^t \frac{d\mathbf{A}(\sigma)}{d\boldsymbol{\theta}} \frac{d\mathcal{L}(\boldsymbol{\theta}(\sigma))}{d\boldsymbol{\theta}} d\sigma \right\|_2 \\ &\leq \frac{2}{\sqrt{d}} \int_0^t \left\| \frac{d\mathbf{A}(\sigma)}{d\boldsymbol{\theta}} \frac{d\mathcal{L}(\boldsymbol{\theta}(\sigma))}{d\boldsymbol{\theta}} \right\|_2 d\sigma, \\ &= \frac{2}{\sqrt{d}} \int_0^t \sqrt{\sum_i^d \left(\frac{dA_i(\sigma)}{db_i} \frac{\partial \mathcal{L}(\boldsymbol{\theta}(\sigma))}{\partial b_i} \right)^2} d\sigma,\end{aligned}\quad (\text{B.27})$$

where

$$\begin{aligned} \frac{dA_i(\sigma)}{db_i} &= -2b_i(\sigma)\varepsilon_i e^{-b_i^2(\sigma)\varepsilon_i}, \\ \frac{\partial \mathcal{L}(\boldsymbol{\theta})}{\partial b_i} &= \sum_j^{n_g} \left(G[u(x_j^g, \boldsymbol{\theta})] - g(x_j^g) \right) \frac{\partial G[u(x_j^g, \boldsymbol{\theta})]}{\partial b_i} + \\ &\quad \sum_j^{n_b} \left(B[u(x_j^b, \boldsymbol{\theta})] - b(x_j^b) \right) \frac{\partial B[u(x_j^b, \boldsymbol{\theta})]}{\partial b_i}. \end{aligned} \quad (\text{B.28})$$

Thus,

$$\begin{aligned} &\frac{2}{\sqrt{d}} \int_0^t \sqrt{\sum_i^d \left(\frac{dA_i(\sigma)}{db_i} \frac{\partial \mathcal{L}(\boldsymbol{\theta}(\sigma))}{\partial b_i} \right)^2} d\sigma, \\ &\leq \frac{2}{\sqrt{d}} \int_0^t \left\| \frac{d\mathbf{A}(\sigma)}{d\mathbf{b}} \right\|_\infty \sum_i^d \sqrt{\left(\frac{\partial \mathcal{L}(\boldsymbol{\theta}(\sigma))}{\partial b_i} \right)^2} d\sigma \\ &\leq H + I, \end{aligned} \quad (\text{B.29})$$

where

$$\begin{aligned} H &= \frac{2}{\sqrt{d}} \int_0^t \left\| \frac{d\mathbf{A}(\sigma)}{d\mathbf{b}} \right\|_\infty \left\| \frac{dG[u(x_j^g)]}{d\mathbf{b}} \right\|_\infty \sqrt{\sum_i^d \left(\sum_j^{n_g} \left(G[u(x_j^g)] - g(x_j^g) \right) \right)^2} d\sigma \\ I &= \frac{2}{\sqrt{d}} \int_0^t \left\| \frac{d\mathbf{A}(\sigma)}{d\mathbf{b}} \right\|_\infty \left\| \frac{dB[u(x_j^b)]}{d\mathbf{b}} \right\|_\infty \sqrt{\sum_i^d \left(\sum_j^{n_b} \left(B[u(x_j^b)] - b(x_j^b) \right) \right)^2} d\sigma \end{aligned} \quad (\text{B.30})$$

Note that [51]

$$\begin{aligned} \left\| \frac{d\mathbf{A}(\sigma)}{d\mathbf{b}} \right\|_\infty &= O\left(\frac{1}{\sqrt{d}}\right), \\ \left\| \frac{dG[u(x_j^g)]}{d\mathbf{b}} \right\|_\infty &= O\left(\frac{1}{\sqrt{d}}\right), \\ \left\| \frac{dB[u(x_j^b)]}{d\mathbf{b}} \right\|_\infty &= O\left(\frac{1}{\sqrt{d}}\right). \end{aligned} \quad (\text{B.31})$$

Hence,

$$\begin{aligned} \lim_{d \rightarrow \infty} \sup_{t \in [0, T]} H &= O\left(\frac{2\mathcal{C}}{d}\right) = 0, \\ \lim_{d \rightarrow \infty} \sup_{t \in [0, T]} I &= O\left(\frac{2\mathcal{C}}{d}\right) = 0, \end{aligned} \quad (\text{B.32})$$

We can conclude that

$$\lim_{d \rightarrow \infty} \sup_{t \in [0, T]} \frac{2}{\sqrt{d}} \|\mathbf{A}(t) - \mathbf{A}(0)\|_2 = 0. \quad (\text{B.33})$$

Similarly, we can prove that

$$\begin{aligned} \lim_{d \rightarrow \infty} \sup_{t \in [0, T]} \frac{2}{\sqrt{d}} \|\mathbf{B}(t) - \mathbf{B}(0)\|_2 &= 0, \\ \lim_{d \rightarrow \infty} \sup_{t \in [0, T]} \frac{2}{\sqrt{d}} \|\mathbf{C}(t) - \mathbf{C}(0)\|_2 &= 0, \\ \lim_{d \rightarrow \infty} \sup_{t \in [0, T]} \frac{2}{\sqrt{d}} \|\mathbf{D}(t) - \mathbf{D}(0)\|_2 &= 0. \end{aligned} \quad (\text{B.34})$$

By Eqs. (B.33) and (B.34), we obtain that

$$\begin{aligned} \lim_{d \rightarrow \infty} \sup_{t \in [0, T]} \left(\frac{2}{\sqrt{d}} \|\mathbf{A}(t) - \mathbf{A}(0)\|_2 + \frac{2}{\sqrt{d}} \|\mathbf{B}(t) - \mathbf{B}(0)\|_2 \right) &\rightarrow 0, \\ \lim_{d \rightarrow \infty} \sup_{t \in [0, T]} \left(\frac{1}{\sqrt{d}} \|\mathbf{C}(t) - \mathbf{C}(0)\|_2 + \frac{1}{\sqrt{d}} \|\mathbf{D}(t) - \mathbf{D}(0)\|_2 \right) &\rightarrow 0. \end{aligned} \quad (\text{B.35})$$

Therefore, we have

$$\lim_{d \rightarrow \infty} \sup_{t \in [0, T]} \|\mathbf{J}(t) - \mathbf{J}(0)\|_2 \rightarrow 0. \quad (\text{B.36})$$

And obviously, one can conclude that

$$\lim_{d \rightarrow \infty} \sup_{t \in [0, T]} \|\mathbf{K}(t) - \mathbf{K}(0)\|_2 \rightarrow 0. \quad (\text{B.37})$$

Appendix C. The analytical solution of Poiseuille flow with the UCM fluid

The analytical solution of the Poiseuille flow problem with the UCM fluid is given as [74]

$$\begin{aligned} u(y, t) &= u_{\max} U(y, t), \\ \tau_{xy}(y, t) &= u_{\max} T_{xy}(y, t) \end{aligned} \quad (\text{C.1})$$

where $u_{\max} = 4h^2 f / (12\eta_0)$ is the mean streamwise velocity. $U(y, t)$ and $T_{xy}(y, t)$ are given as

$$\begin{aligned} U(y, t) &= 1.5(1 - 4y^2) - 48 \sum_{i=1}^{\infty} \frac{\sin(0.5N_i(2y+1))}{N_i^3} e^{-0.5t/\lambda} G_i(t), \\ T_{xy}(y, t) &= -6Y + 48 \sum_{i=1}^{\infty} \frac{\cos(0.5N_i(2y+1))}{N_i} e^{-0.5t/\lambda} Q_i(t), \end{aligned} \quad (\text{C.2})$$

where

$$\begin{aligned} G_i(t) &= \cosh\left(\frac{\beta_i t}{2\lambda}\right) + \frac{\gamma_i}{\beta_i} \sinh\left(\frac{\beta_i t}{2\lambda}\right), \\ Q_i(t) &= -\frac{\alpha}{EN_i^3} G_i(t) + \frac{2}{\lambda EN_i^3} \frac{\partial}{\partial t} G_i(t), \end{aligned} \quad (\text{C.3})$$

and

$$\begin{aligned} \beta_i &= \sqrt{EN_i^2 - 1}, \gamma_i = 1 - 0.5EN_i^2, \\ N_i &= (2i-1)\pi, E = \frac{\lambda\eta_0}{\rho h^2}. \end{aligned} \quad (\text{C.4})$$

References

- [1] C. Beck, M. Hutzenthaler, A. Jentzen, B. Kuckuck, An overview on deep learning-based approximation methods for partial differential equations, 2020, arXiv preprint [arXiv:12348](https://arxiv.org/abs/12348).
- [2] G.E. Karniadakis, I.G. Kevrekidis, L. Lu, P. Perdikaris, S. Wang, L. Yang, Physics-informed machine learning, Nat. Rev. Phys. 3 (2021) 422–440.
- [3] J. Bai, L. Alzubaidi, Q. Wang, E. Kuhl, M. Bennamoun, Y. Gu, Utilising physics-guided deep learning to overcome data scarcity, 2022, arXiv preprint [arXiv:2211.15664](https://arxiv.org/abs/2211.15664).

- [4] E. Samaniego, C. Anitescu, S. Goswami, V.M. Nguyen-Thanh, H. Guo, K. Hamdia, X. Zhuang, T. Rabczuk, An energy approach to the solution of partial differential equations in computational mechanics via machine learning: Concepts, implementation and applications, *Comput. Methods Appl. Mech. Engrg.* 362 (2020).
- [5] V.M. Nguyen-Thanh, X. Zhuang, T. Rabczuk, A deep energy method for finite deformation hyperelasticity, *Eur. J. Mech. A Solids* 80 (2020) 103874.
- [6] W. Li, M.Z. Bazant, J. Zhu, A physics-guided neural network framework for elastic plates: Comparison of governing equations-based and energy-based approaches, *Comput. Methods Appl. Mech. Engrg.* 383 (2021) 113933.
- [7] E. Haghighat, M. Raissi, A. Moure, H. Gomez, R. Juanes, A physics-informed deep learning framework for inversion and surrogate modeling in solid mechanics, *Comput. Methods Appl. Mech. Engrg.* 379 (2021) 113741.
- [8] X. Zhuang, H. Guo, N. Alajlan, H. Zhu, T. Rabczuk, Deep autoencoder based energy method for the bending, vibration, and buckling analysis of Kirchhoff plates with transfer learning, *Eur. J. Mech. A Solids* 87 (2021) 104225.
- [9] A. Henkes, H. Wessels, R. Mahnken, Physics informed neural networks for continuum micromechanics, *Comput. Methods Appl. Mech. Engrg.* 393 (2022) 114790.
- [10] S. Rezaei, A. Harandi, A. Moeinuddin, B.-X. Xu, S. Reese, A mixed formulation for physics-informed neural networks as a potential solver for engineering problems in heterogeneous domains: Comparison with finite element method, *Comput. Methods Appl. Mech. Engrg.* 401 (2022).
- [11] J. Bai, Y. Zhou, Y. Ma, H. Jeong, H. Zhan, C. Rathnayaka, E. Sauret, Y. Gu, A general neural particle method for hydrodynamics modeling, *Comput. Methods Appl. Mech. Engrg.* 393 (2022) 114740.
- [12] H. Wessels, C. Weißenfels, P. Wriggers, The neural particle method – an updated Lagrangian physics informed neural network for computational fluid dynamics, *Comput. Methods Appl. Mech. Engrg.* 368 (2020) 113127.
- [13] M. Raissi, A. Yazdani, G.E. Karniadakis, Hidden fluid mechanics: Learning velocity and pressure fields from flow visualizations, *Science* 367 (2020) 1026–1030.
- [14] S. Cai, Z. Wang, F. Fuest, Y.J. Jeon, C. Gray, G.E. Karniadakis, Flow over an espresso cup: Inferring 3-D velocity and pressure fields from tomographic background oriented Schlieren via physics-informed neural networks, *J. Fluid Mech.* 915 (2021) A102.
- [15] Z. Li, J. Bai, H. Ouyang, S. Martelli, M. Tang, H. Wei, P. Liu, W.-R. Han, Y. Gu, Physics-informed neural network for friction-involved nonsmooth dynamics problems, 2023, arXiv preprint [arXiv:02542](https://arxiv.org/abs/2301.02542).
- [16] A. Ghaderi, V. Morovati, Y. Chen, R. Dargazany, A physics-informed multi-agents model to predict thermo-oxidative/hydrolytic aging of elastomers, *Int. J. Mech. Sci.* 223 (2022).
- [17] J. Wu, L. Bai, J. Huang, L. Ma, J. Liu, S. Liu, Accurate force field of two-dimensional ferroelectrics from deep learning, *Phys. Rev. B* 104 (2021).
- [18] W. Li, J. Zhang, F. Ringbeck, D. Jöst, L. Zhang, Z. Wei, D.U. Sauer, Physics-informed neural networks for electrode-level state estimation in lithium-ion batteries, *J. Power Sources* 506 (2021).
- [19] Y. Chen, L. Lu, G.E. Karniadakis, L. Dal Negro, Physics-informed neural networks for inverse problems in nano-optics and metamaterials, *Opt. Express* 28 (2020) 11618–11633.
- [20] L. Zhang, J. Han, H. Wang, R. Car, W. E, Deep potential molecular dynamics: A scalable model with the accuracy of quantum mechanics, *Phys. Rev. Lett.* 120 (2018) 143001.
- [21] H. Wang, L. Zhang, J. Han, W. E, DeePMD-kit: A deep learning package for many-body potential energy representation and molecular dynamics, *Comput. Phys. Comm.* 228 (2018) 178–184.
- [22] J. Tian, R. Xiong, J. Lu, C. Chen, W. Shen, Battery state-of-charge estimation amid dynamic usage with physics-informed deep learning, *Energy Storage Mater.* 50 (2022) 718–729.
- [23] M. Yin, X. Zheng, J.D. Humphrey, G. Em Karniadakis, Non-invasive inference of thrombus material properties with physics-informed neural networks, *Comput. Methods Appl. Mech. Engrg.* 375 (2021).
- [24] G. Kissas, Y. Yang, E. Hwang, W.R. Witschey, J.A. Detre, P. Perdikaris, Machine learning in cardiovascular flows modeling: Predicting arterial blood pressure from non-invasive 4D flow MRI data using physics-informed neural networks, *Comput. Methods Appl. Mech. Engrg.* 358 (2020).
- [25] K. Linka, A. Schäfer, X. Meng, Z. Zou, G.E. Karniadakis, E. Kuhl, Bayesian physics informed neural networks for real-world nonlinear dynamical systems, *Comput. Methods Appl. Mech. Engrg.* (2022).
- [26] D.R. Rutkowski, A. Roldan-Alzate, K.M. Johnson, Enhancement of cerebrovascular 4D flow MRI velocity fields using machine learning and computational fluid dynamics simulation data, *Sci. Rep.* 11 (2021) 10240.
- [27] E. Kharazmi, M. Cai, X. Zheng, Z. Zhang, G. Lin, G.E. Karniadakis, Identifiability and predictability of integer- and fractional-order epidemiological models using physics-informed neural networks, *Nat. Comput. Sci.* 1 (2021) 744–753.
- [28] M.P.T. Kaandorp, S. Barbieri, R. Klaassen, H.W.M. van Laarhoven, H. Crezee, P.T. While, A.J. Nederveen, O.J. Gurney-Champion, Improved unsupervised physics-informed deep learning for intravoxel incoherent motion modeling and evaluation in pancreatic cancer patients, *Magn. Reson. Med.* 86 (2021) 2250–2265.
- [29] S. Cai, H. Li, F. Zheng, F. Kong, M. Dao, G.E. Karniadakis, S. Suresh, Artificial intelligence velocimetry and microaneurysm-on-a-chip for three-dimensional analysis of blood flow in physiology and disease, *Proc. Natl. Acad. Sci. USA* 118 (2021).
- [30] S. Buoso, T. Joyce, S. Kozerke, Personalising left-ventricular biophysical models of the heart using parametric physics-informed neural networks, *Med. Image. Anal.* 71 (2021) 102066.
- [31] J.H. Lagergren, J.T. Nardini, R.E. Baker, M.J. Simpson, K.B. Flores, Biologically-informed neural networks guide mechanistic modeling from sparse experimental data, *PLoS Comput. Biol.* 16 (2020) e1008462.
- [32] F. Sahli Costabal, Y. Yang, P. Perdikaris, D.E. Hurtado, E. Kuhl, Physics-informed neural networks for cardiac activation mapping, *Front. Phys.* 8 (2020).

- [33] A. Rodríguez, J. Cui, N. Ramakrishnan, B. Adhikari, B.A. Prakash, EINNs: Epidemiologically-informed neural networks, 2022, arXiv preprint [arXiv:10446](https://arxiv.org/abs/2201.10446).
- [34] M.A. Bhouri, F.S. Costabal, H. Wang, K. Linka, M. Peirlinck, E. Kuhl, P. Perdikaris, Covid-19 dynamics across the US: A deep learning study of human mobility and social behavior, *Comput. Methods Appl. Mech. Engrg.* 382 (2021).
- [35] S. Wang, Y. Teng, P. Perdikaris, Understanding and mitigating gradient pathologies in physics-informed neural networks, 2020, arXiv preprint [arXiv:04536](https://arxiv.org/abs/2004.04536).
- [36] H. Jeong, J. Bai, C.P. Batuwatta-Gamage, C. Rathnayaka, Y. Zhou, Y. Gu, A physics-informed neural network-based topology optimization (PINNTO) framework for structural optimization, *Eng. Struct.* 278 (2023).
- [37] E. Kharazmi, Z. Zhang, G.E.M. Karniadakis, hp-VPINNs: Variational physics-informed neural networks with domain decomposition, *Comput. Methods Appl. Mech. Engrg.* 374 (2021) 113547.
- [38] E. Haghighat, A.C. Bekar, E. Madenci, R. Juanes, A nonlocal physics-informed deep learning framework using the peridynamic differential operator, *Comput. Methods Appl. Mech. Engrg.* 385 (2021) 114012.
- [39] J. Yu, L. Lu, X. Meng, G.E. Karniadakis, Gradient-enhanced physics-informed neural networks for forward and inverse PDE problems, *Comput. Methods Appl. Mech. Engrg.* 393 (2022).
- [40] J.N. Fuhr, N. Bouklas, The mixed deep energy method for resolving concentration features in finite strain hyperelasticity, *J. Comput. Phys.* 451 (2021) 110839.
- [41] J. Bai, T. Rabczuk, A. Gupta, L. Alzubaidi, Y. Gu, A physics-informed neural network technique based on a modified loss function for computational 2D and 3D solid mechanics, *Comput. Mech.* 71 (2022) 543–562.
- [42] A.D. Jagtap, E. Kharazmi, G.E. Karniadakis, Conservative physics-informed neural networks on discrete domains for conservation laws: Applications to forward and inverse problems, *Comput. Methods Appl. Mech. Engrg.* 365 (2020) 113028.
- [43] S. Dong, Z. Li, Local extreme learning machines and domain decomposition for solving linear and nonlinear partial differential equations, *Comput. Methods Appl. Mech. Engrg.* 387 (2021) 114129.
- [44] K. Shukla, A.D. Jagtap, G.E. Karniadakis, Parallel physics-informed neural networks via domain decomposition, *J. Comput. Phys.* 447 (2021) 110683.
- [45] V.M. Nguyen-Thanh, C. Anitescu, N. Alajlan, T. Rabczuk, X. Zhuang, Parametric deep energy approach for elasticity accounting for strain gradient effects, *Comput. Methods Appl. Mech. Engrg.* 386 (2021) 114096.
- [46] A.A. Ramabathiran, P. Ramachandran, SPINN: Sparse, physics-based, and partially interpretable neural networks for PDEs, *J. Comput. Phys.* 445 (2021) 110600.
- [47] A. Jacot, F. Gabriel, C. Hongler, Neural tangent kernel: Convergence and generalization in neural networks, *Proc. Adv. Neural Inf. Process. Syst.* (2018).
- [48] Y. Chen, B. Hosseini, H. Owhadi, A.M. Stuart, Solving and learning nonlinear PDEs with Gaussian processes, *J. Comput. Phys.* 447 (2021) 110668.
- [49] S.S. Du, X. Zhai, B. Poczos, A. Singh, Gradient descent provably optimizes over-parameterized neural networks, 2018, arXiv preprint [arXiv:02054](https://arxiv.org/abs/1806.02054).
- [50] S.S. Du, J. Lee, H. Li, L. Wang, X. Zhai, Gradient descent finds global minima of deep neural networks, in: Proceedings of the 36th International Conference on Machine Learning, Proceedings of Machine Learning Research, PMLR, 2019, pp. 1675–1685.
- [51] S. Wang, X. Yu, P. Perdikaris, When and why PINNs fail to train: A neural tangent kernel perspective, *J. Comput. Phys.* 449 (2021) 110768.
- [52] S. Wang, H. Wang, P. Perdikaris, On the eigenvector bias of Fourier feature networks: From regression to solving multi-scale PDEs with physics-informed neural networks, *Comput. Methods Appl. Mech. Engrg.* 384 (2021) 113938.
- [53] S. Wang, P. Perdikaris, Long-time integration of parametric evolution equations with physics-informed DeepONets, *J. Comput. Phys.* (2022).
- [54] Y. Li, S. Guo, Z. Gan, Empirical prior based probabilistic inference neural network for policy learning, *Inform. Sci.* 615 (2022) 678–699.
- [55] C. Xu, B.T. Cao, Y. Yuan, G. Meschke, Transfer learning based physics-informed neural networks for solving inverse problems in engineering structures under different loading scenarios, *Comput. Methods Appl. Mech. Engrg.* 405 (2023).
- [56] M. Raissi, P. Perdikaris, G.E. Karniadakis, Physics-informed neural networks: A deep learning framework for solving forward and inverse problems involving nonlinear partial differential equations, *J. Comput. Phys.* 378 (2019) 686–707.
- [57] Z. Lin, V. Sekar, G. Fanti, Why spectral normalization stabilizes gans: Analysis and improvements, *Adv. Neural Inf. Process. Syst.* 34 (2021) 9625–9638.
- [58] Y. Bengio, I. Goodfellow, A. Courville, Deep Learning, MIT Press, Massachusetts, USA, 2017.
- [59] D.S. Broomhead, D. Lowe, Radial basis functions, multi-variable functional interpolation and adaptive networks, in: Royal Signals and Radar Establishment, Malvern, United Kingdom, 1988.
- [60] G.-R. Liu, Y. Gu, An Introduction to Meshfree Methods and their Programming, Springer Science & Business Media, 2005.
- [61] B. Bordelon, A. Canatar, C. Pehlevan, Spectrum dependent learning curves in kernel regression and wide neural networks, in: International Conference on Machine Learning, PMLR, 2020, pp. 1024–1034.
- [62] C. Anitescu, E. Atroshchenko, N. Alajlan, T. Rabczuk, Artificial neural network methods for the solution of second order boundary value problems, *Comput. Mater. Contin.* 59 (2019).
- [63] C. Wu, M. Zhu, Q. Tan, Y. Kartha, L. Lu, A comprehensive study of non-adaptive and residual-based adaptive sampling for physics-informed neural networks, *Comput. Methods Appl. Mech. Engrg.* 403 (2023) 115671.
- [64] C. Zhang, M. Rezavand, Y. Zhu, Y. Yu, D. Wu, W. Zhang, J. Wang, X.J.C.P.C. Hu, SPHinXsys: An Open-Source Multi-Physics and Multi-Resolution Library Based on Smoothed Particle Hydrodynamics, vol. 267, 2021, p. 108066.

- [65] C.P. Batuwatta-Gamage, C.M. Rathnayaka, H.C.P. Karunasena, W.D.C.C. Wijerathne, H. Jeong, Z.G. Welsh, M.A. Karim, Y.T. Gu, A physics-informed neural network-based surrogate framework to predict moisture concentration and shrinkage of a plant cell during drying, *J. Food Eng.* 332 (2022).
- [66] M.A. Alves, P.J. Oliveira, F.T. Pinho, Numerical methods for viscoelastic fluid flows, *Annu. Rev. Fluid Mech.* 53 (2021) 509–541.
- [67] S. Goswami, C. Anitescu, S. Chakraborty, T. Rabczuk, Transfer learning enhanced physics informed neural network for phase-field modeling of fracture, *Theor. Appl. Fract. Mech.* 106 (2020) 102447.
- [68] X. Liu, G. Liu, K. Tai, Radial point interpolation collocation method (RPICM) using upwind biased local support scheme for solving convection-dominated equations, in: *Computational Methods*, Springer, 2006, pp. 1541–1546.
- [69] X. Liu, G. Liu, K. Tai, K. Lam, Radial point interpolation collocation method (RPICM) for partial differential equations, *Comput. Math. Appl.* 50 (2005) 1425–1442.
- [70] X. Liu, G. Liu, K. Tai, K. Lam, Radial point interpolation collocation method (RPICM) for the solution of nonlinear Poisson problems, *Comput. Mech.* 36 (2005) 298–306.
- [71] G.-R. Liu, *Mesh Free Methods: Moving beyond the Finite Element Method*, CRC Press, 2003.
- [72] G.-R. Liu, *Machine Learning with Python: Theory and Applications*, World Scientific, 2022.
- [73] J. Wang, G. Liu, On the optimal shape parameters of radial basis functions used for 2-D meshless methods, *Comput. Methods Appl. Mech. Eng.* 191 (2002) 2611–2630.
- [74] S.C. Xue, R.I. Tanner, N. Phan-Thien, Numerical modelling of transient viscoelastic flows, *J. Non-Newton. Fluid Mech.* 123 (2004) 33–58.